March 2001 • NREL/SR-520-29956

Subcontractor Report

Process Development and Basic Studies of Electrochemically Deposited CdTe-Based Solar Cells

Annual Technical Report, Phase II
16 May 1999–13 May 2000

V. I. Kaydanov and T. R. Ohno
Colorado School of Mines
Golden, Colorado

National Renewable Energy Laboratory

1617 Cole Boulevard
Golden, Colorado 80401-3393

NREL is a U.S. Department of Energy Laboratory
Operated by Midwest Research Institute • Battelle • Bechtel

Contract No. DE-AC36-99-GO10337

March 2001 • NREL/SR-520-29956

Process Development and Basic Studies of Electrochemically Deposited CdTe-Based Solar Cells

Annual Technical Report, Phase II 16 May 1999–13 May 2000

V. I. Kaydanov and T. R. Ohno
Colorado School of Mines
Golden, Colorado

NREL Technical Monitor: Bolko von Roedern

Prepared under Subcontract No. XAK-8-17619-28

National Renewable Energy Laboratory

1617 Cole Boulevard
Golden, Colorado 80401-3393

NREL is a U.S. Department of Energy Laboratory
Operated by Midwest Research Institute • Battelle • Bechtel

Contract No. DE-AC36-99-GO10337

NOTICE

Available electronically at http://www.doe.gov/bridge

Available for a processing fee to U.S. Department of Energy
and its contractors, in paper, from:

U.S. Department of Energy
Office of Scientific and Technical Information
P.O. Box 62
Oak Ridge, TN 37831-0062
phone: 865.576.8401
fax: 865.576.5728
email: reports@adonis.osti.gov

Available for sale to the public, in paper, from:

U.S. Department of Commerce
National Technical Information Service
5285 Port Royal Road
Springfield, VA 22161
phone: 800.553.6847
fax: 703.605.6900
email: orders@ntis.fedworld.gov
online ordering: http://www.ntis.gov/ordering.htm

Printed on paper containing at least 50% wastepaper, including 20% postconsumer waste

Preface

This project, "Process Development and Basic Studies of Electrochemically Deposited CdTe-Based Solar Cells", which is performed at the Colorado School of Mines (CSM), is part of the NREL Thin-Film Partnership Program. The project addresses long-term research and development issues related to polycrystalline thin-film solar cells. Our general research approach is based on combining activities aimed at improvement of cell performance and stability with activities aimed at increasing our fundamental understanding of the properties of materials making up the cells: CdTe, CdS, multi-layer back contact, and transparent conducting oxide (TCO) front contact. We emphasize the relation between structural and electronic material properties and various processing procedures as well as the microscopic mechanisms responsible for the cell performance and its degradation.

There is a lack of knowledge and understanding of basic issues behind the CdTe/CdS cells performance and stability, such as nature and electronic properties of impurities and defects that control the majority carrier concentration, mechanisms of the dopant compensation, recombination centers, their nature and properties, diffusion, electromigration and transformation of defects under various processing, stress, and operating conditions, etc. We believe that better basic understanding of the specific influence of polycrystallinity, especially for fine-grain materials like those making up CdTe-based cells, is now one of the most important issues we must address. We need to clarify the role of grain boundaries (GB) in forming the film electronic properties as well as those of the p-n junction. It is important to study and understand the influence of the GB boundaries on the spatial distribution and migration of impurities and electrically active defects. To fulfill these tasks one needs to develop new methods and techniques (or adjust existing ones) for material characterization as well as more sophisticated approaches to the data analysis and modeling. This report presents studies relevant to the problems formulated above that were carried out at CSM at Phase II of the project according to the Statement of Work and Tasks of the Subcontract.

Section 1 presents studies of degradation under stressing of the cells with differently processed CdTe and different back contacts. We compared cells based on CdTe prepared by First Solar, LLC, and on CdTe electrodeposited at CSM. Back contacts were of two types: Cu/ZnTe/Au and Cu/Au. It was shown that under the same stress conditions the degradation of the cell parameters occurs significantly different for the cells with differently prepared CdTe as well as for different back contacts. Degradation of cells was accompanied and caused, at least partially, by significant changes in doping profile which indicates spatial redistribution of electrically active defects and probably non-uniform changes in compensation degree. A strong influence of bias applied during stressing on the doping profile can be attributed to a significant contribution of electromigration to this and perhaps to transformation of the defects in strong electric fields. The section is concluded with an analysis of the problems to be addressed in continuing studies, including the acceptor levels and compensating defects, deep traps, influence of grain boundaries, and deep traps. The following sections present some of our studies performed at Phase II aimed at development and checking the validity of the approaches and methods we use for studies of basic properties of the cells and their thin film constituents.

Section 2 presents studies of deep traps in the electrodeposited CdTe cells performed in collaboration with NREL. For characterization of the cells a variety of methods were used. Along with routine J-V and C-V measurements, the C(V,T), C(V, f), DLTS, were also used. It was found

that the C-V profile changes significantly with temperature. Two possible mechanisms behind these changes were discussed: (a) the temperature dependence of the free hole concentration (due to not too shallow acceptor levels and maybe to strong compensation), and (b) high concentration of deep traps, whose contribution to the measured capacitance increases with temperature. The second mechanism was verified by a strong dependence of capacitance on the testing voltage frequency. One deep trap for electrons and four traps for holes were detected by DLTS studies. The estimated concentration of traps is comparable to the free hole concentration detected by C-V measurements and depends strongly on the temperature of the Cu post-deposition annealing temperature. The latter also influences Cu concentration detected by SIMS measurements. It was found that the minority-carrier lifetime reduces with increasing concentration of Cu and of the traps located close to midgap.

Studies of spectral dependencies of photocurrent and its spatial distribution over the cross section of the ED CdTe cell were performed using the near field scanning optical microscopy (NSOM) (Sec. 3). The instrumentation provided spatial resolution of ~1000 Å which was sufficient for revealing and mapping non-uniformities caused by the fine-granular structure of the CdTe absorber layer. Dependence of the $CdTe_{1-x}S_x$ bandgap on S composition enabled the microscopic identification of S-rich regions in the CdTe layer by combining NSOM with a tunable laser. S composition was found to be very non-uniform and greater along grain boundaries than in the grain centers, identifying grain boundaries as locations of enhanced interdiffusion. In some cross-sectional photocurrent images, enhancements in photocurrent were observed near grain boundaries for the photon energies not only below but also well above the CdTe bandgap. This non-trivial effect may provide some guidance about the complex influence of grain boundaries on cell performance.

Impedance spectroscopy of CdTe and CdS thin films is discussed in Section 4. Measurements of the complex impedance in polycrystalline films are aimed at studies of electronic properties of grain boundaries. Based on results obtained in Phase II more complex physical and electrical models were developed for experimental data analysis. Some technical problems of measurements are discussed in this section as well as their possible solutions. The results of the impedance spectroscopy studies on CdTe films with different processing stages show a dependence of the GB properties on processing technology.

Studies of band spectrum and electron scattering in transparent conducting oxides are presented in Section 5. We discuss here details and parameters of the spectrum and scattering that relate to the figure of merit TCOs, formulate and theoretically ground an experimental method based on simultaneous measurements of four transport coefficients: electrical resistivity, Hall, Seebeck, and Nernst-Ettingshausen coefficients. Combined with measurements of plasma and collision frequencies (ultra-high frequency electron transport) this method provides information on the effective mass value, deviation from a parabolic spectrum, the shape of constant-energy surfaces, dominating scattering mechanism, and also on contribution of grain boundaries to the film sheet resistance. A brief description of principal features of the measurement equipment and experimental procedure are presented in this section which is concluded with a review of results obtained so far for some TCO materials.

Appendices present data on personnel involved in the studies, laboratory improvements, and publications.

Table of Contents

List of Figures

List of Tables

1. Comparison of Degradation in Vapor Transport- and Electro- Deposited CdTe Solar Cells with ZnTe:Cu/Au and Cu/Au Back Contacts

1.1 Introduction

Almost all groups working on CdTe solar cells have used Cu-doping of CdS/CdTe solar cells via back contact application. The positive effect of Cu mainly comes from enhancement of V_{oc} and FF, the latter due to a significant decrease in the back contact resistance. While copper improves the initial performance of CdS/CdTe solar cells, it was found in many studies to deteriorate the cell stability [1, 2]. It is believed that one of the reasons is fast diffusion and electromigration of Cu in CdTe, especially along grain boundaries in polycrystalline films. That leads to expectation that morphology of CdTe film should impact Cu migration and degradation process. Indeed, degradation rates under different stress conditions and their peculiarities reported by various groups are different depending on the processing techniques, type and application method of the back contact. Studies presented in this section were aimed at clarifying some of these issues.

1.2 Experimental

Two types of CdS/CdTe structures were used in this study. One was provided by First Solar, LLC, (FS). It contains about 300 nm thick CdS and wet $CdCl_2$ treated 3.5 to 4.0 μm thick CdTe prepared with the gas transport deposition method. The other type was prepared at Colorado School of Mines (CSM), containing 250 nm thick CdS (prepared with chemical bath deposition, CBD) and electrodeposited 3.3 μm thick CdTe. A wet $CdCl_2$ treatment was given to both CdS and CdTe [3].

Two types of back contacts were applied to the FS materials: ZnTe:Cu/Au and Cu/Au. For the first one, thin layers of Cu (7Å) and ZnTe (500Å) were evaporated on Br_2/methanol etched CdTe, and annealed in N_2 prior to evaporation of gold through mask to complete the back contact. For the second a thin Cu layer (30Å) was evaporated on the Br_2/methanol etched surface of CdTe and annealed in N_2. The excess Cu was removed by etching in Br_2/methanol solution, and Au was evaporated to complete the back contact. Cells on the CSM material were completed only with the Cu/Au back contact.

All three types of cells were stressed in dark at 100^0C in air under three bias conditions: open circuit (OC), forward bias of 0.55V (FB), and reverse bias of –1.2V (RB). Cells were periodically taken out of the oven and cooled down to room temperature before characterizing with I-V and C-V (at 100 kHz) techniques.

1.3 Results

Fig. 1.1 shows the efficiency degradation under FB and RB conditions for the three types of cells: First Solar material (FS) with the first (Cu/ZnTe/Au) and the second (Cu/Au) types of back contact, and the CSM electrodeposited (ED) CdTe with the Cu/Au back contact. Cells stressed under FB (with any back contact) demonstrate the least degradation. FS-ZnTe cells show a

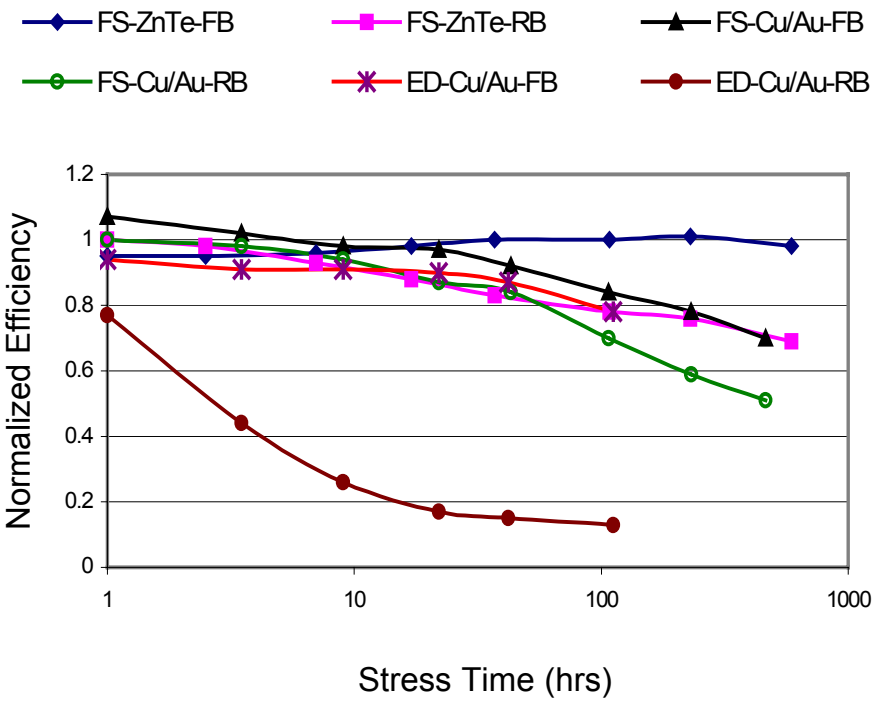

Fig. 1.1 Changes in normalized efficiency with stress time

decrease in efficiency by only 3% in 590 stressing hours while OC (not shown in the Figure) provided a 6% decrease for the same stressing time, and RB shows the most severe degradation of 33%. FS-Cu/Au samples show higher degree of degradation than that of the Cu/ZnTe/Au samples and different trend in efficiency change with time. Degradation is much more severe in the CSM (ED-Cu/Au) cells for all bias conditions, with the efficiency decreased by 80% under RB within 22 hours.

The trends in efficiency change in the initial hours of stressing are quite different for different back contacts. FS-ZnTe cells stressed under FB first manifest a decrease in efficiency by 6% (higher than decrease in 590 hours), followed by an increase. The trend is opposite for the same samples stressed under OC with the initial increase in efficiency followed by decrease. Cu/Au back contact on the FS material manifests different trends. FB stressed cells show an initial increase in efficiency followed by a decrease, while OC-stressed cells show continuous decrease. Only reverse-biased cells showed almost the same trends of continuous decrease in both cases.

Pictograms in Fig.1.2 demonstrate visible differences in degradation of Voc and FF for various cells due to different bias conditions. Differences in doping-depth profile changes after stressing correlate with the differences in degradation of the cell parameters. Fig.1.3 shows some data for FS-ZnTe and ED-Cu/Au samples after 110 hours stressing as compared to the initial profiles. There are two major features: (1) Doping density decreases after OC and FB stressing while it

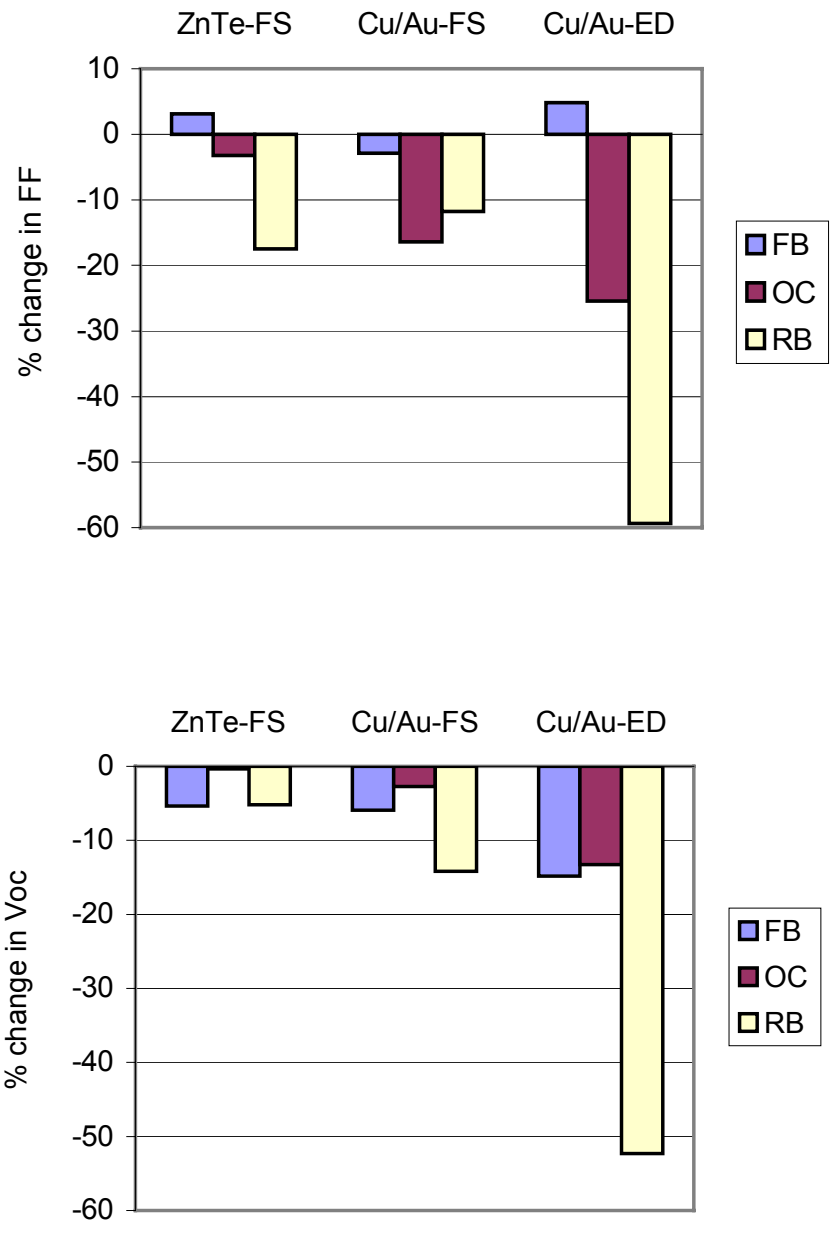

Fig. 1.2. Percentage change in FF and Voc after 110 hours of stressing

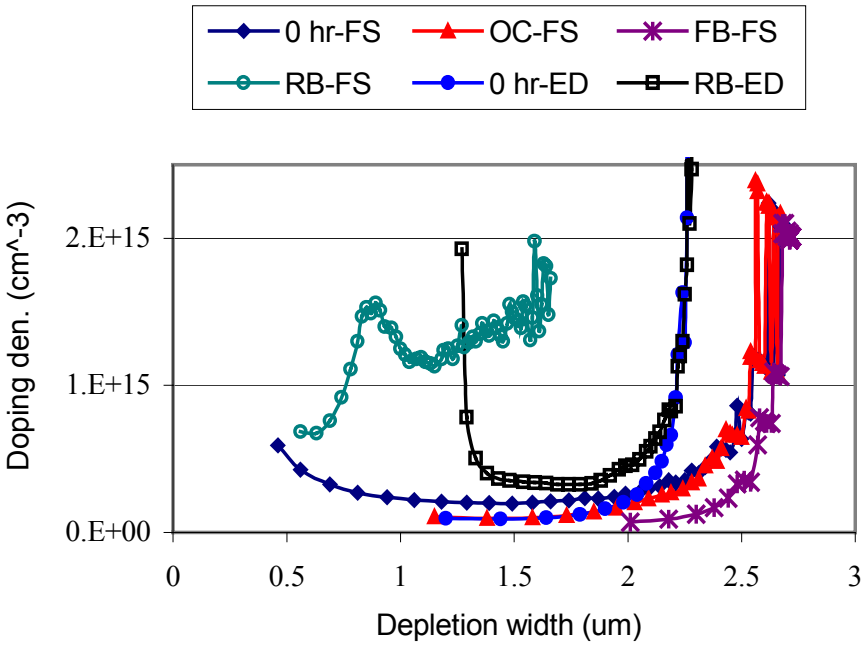

Fig. 1.3. Changes in doping profile for the FS-ZnTe and the CSM (ED) cells after 110 hours of stressing

increases after RB stressing. This correlates with changes in the depletion width derived from the zero bias capacitance. (2) RB stressing causes a peak in doping profile just at the depletion layer edge.

1.4 Discussion

We do not present in this report all the results obtained so far when studying degradation under different stress conditions. It seems that the data presented above are sufficient to formulate the following, rather general, conclusions:

1. The influence of the back contact type on the cell degradation and on changes in doping profile indicates that the Cu-related degradation process depends on the back contact structure. It should be concluded that the role of the ZnTe interlayer is not limited to providing low back contact resistance. Probably its presence also controls the Cu content and distribution throughout the cell.

2. For the same back contact, degradation varies with the CdTe processing. Presumably it occurs due to differences in the film morphology and the grain boundary properties as well as in imperfection of the intra-grain material.

3. Degradation of cells is accompanied and caused, at least partially, by significant changes in doping profile, which indicates spatial redistribution of electrically active defects. A strong influence of the applied bias during stressing should be attributed to a significant contribution of electromigration to this redistribution and maybe also to transformation of the defects in strong electric fields.

We are continuing stress experiments by broadening the variety of stress conditions and their combinations (light, dark, temperature, bias applied). In phase III we plan to study degradation in the cells fabricated with other processing techniques, such as CSS CdTe, APCVD CdTe, and sputtered CdS. These studies will provide richer and more detailed information for discussion of possible mechanisms of degradation.

However, we believe that it is even more important to study in more detail structural and electronic properties of the cells and their changes with varying processing procedures and due to stress testing. Only in this way we will be able to provide a solid scientific basis for clarifying the degradation mechanisms. Below we present some problems we are focussed on.

1. One of the high priority issues is the problem of the electrically active centers that determine the majority carrier concentration. Doping with Cu is commonly used to control the hole concentration in CdTe, but its concentration in CdTe detected by SIMS [4, 5] is orders of magnitude higher than the hole concentration provided by C-V profiling. This discrepancy is not specific for some processing method but is common for all. The major questions to be addressed are:

   (a) What Cu-related defects dominate creation of free holes in CdTe: Cu_{Cd}, Cu-contained complexes, or acceptor-type native defects whose concentration depends on presence and concentration of Cu?

   (b) What are the energy levels provided by the dominating acceptor centers: are those levels shallow or not, in other words, are they completely thermally ionized at room temperature or not? Most reports attribute the acceptor level of E_A-E_V ~ 0.3-0.35 eV found in CdTe:Cu to Cu_{Cd}. This level is deep enough to be much less than half thermally ionized at T=300 K, if the concentration of the centers exceeds 10^{14}cm^{-3}. For example, if E_A-E_V=0.35 eV and $N_{Cu_{Cd}} \approx 10^{16}$ cm^{-3}, the estimated free hole concentration at T=300K should be of $n_h \approx 5\times10^{14}$ cm^{-3}.

   (c) Does a huge difference between N_{Cu} and n_h comes from involvement of the majority of Cu atoms in some neutral precipitates or neutral complexes? Or is there a high degree compensation of the acceptor centers by donor centers provided by Cu_i, or native defects or some complexes? For the shallow acceptors $n_h = N_A - N_D$, hence if $n_h << N_A$, the compensation degree is close to unity ($N_D / N_A \approx 1$). Even a small change in the ratio

N_D /N_A can lead to a significant, by orders, change in the free hole concentration. It should be mentioned that in the case of deep dominating acceptors, the influence of compensation on the hole concentration could be even stronger than for shallow acceptors. For the deep acceptor like that in the example above (E_A-E_V=0.35 eV), $n_h \approx 2\times10^{13}$cm^{-3}, if N_A τ 10^{15}cm^{-3} and N_D /$N_A \approx 0.5$, no matter what is the real N_A value. Variation of the N_D /N_A value impacts the hole concentration much weaker than in the previous case, unless this ratio comes close to either 0 or 1.

(d) What is the influence of the deep electronic states associated with grain boundaries (GB) on the hole concentration in CdTe? Previous studies of the CdTe bicrystals [6] and polycrystalline thin films [7, 8] showed that in the latter with a grain size of ~ 1 μ, the number of the GB states per unit volume can be as high as 10^{16} to 10^{17}cm^{-3}. That means that the GB states can effectively compensate acceptors in the grain volume (deplete the grain bulk). The difference between this compensation mechanism and that considered above is that in the previous case the film is overall as well as locally neutral, while in the latter case grain boundaries are charged positively and the grain bulk is charged negatively, so that film is neutral as a whole but not locally. It should be mentioned that in the case of dominating compensation by the GB states, the negative space charge density in the GB proximity, should be close to N_A and can be much higher than the free hole concentration derived from the C-V profile. Thus the enhanced space charge density (□10×10^{17}cm^{-3}) in the GB region observed in [7, 8] may be explained in particular by the GB compensation mechanism, although accumulation of the acceptor-type defects in the GB region also cannot be excluded.

(e) Another important issue to be addressed is the presence of deep traps and their influence on recombination processes. Although a few publications are devoted to detection and studies of deep traps in CdTe, e.g., [9-12], the problem is far from clear. Numerous deep trap levels were reported so far, but the centers responsible for them have not been identified unambiguously. The sets of the deep levels reported in different publications are not the same and depend on the processing technology, postdeposition treatment, and morphology of polycrystalline films. That leads to an additional uncertainty in identification of the centers. One may expect that some of deep levels detected in the thin film CdTe-based solar cells originate from the CdTe/CdS interface and from the GB's inside the CdTe layer.

2. If one believes that a high compensation degree takes place in CdTe, it is reasonable to expect deep traps of high concentration, higher than the free hole concentration. These traps can influence the magnitude and spatial distribution of the space charge, hence the "doping level"- depth profile obtained with the standard analysis of C-V measurements. It is believed that GB affect strongly the cell performance. The role and mechanisms of their influence on the electronic properties of thin film CdTe solar cells are not understood properly. Here we will discuss some of them:

(a) Presence of potential barriers for the majority carriers at the GB was demonstrated both for the CdTe bicrystals and polycrystalline films, see e.g., [6-8]. That means two- or three-dimensional non-uniformity in the electrostatic potential distribution, hence rather

non-uniform electron transport in thin-film CdTe cells. Potential relief separates spatially electrons and holes reducing the recombination rate. On the other hand, deep GB states that are responsible for the potential barriers can act themselves as the recombination centers.

(b) Diffusion of impurities and defects may be expected to be faster along the grain boundaries. This expectation was verified for interdiffusion at the CdTe/CdS interface [13, 14]. It was shown, although indirectly, that concentration of the ternary phase and the S content is higher in the GB regions. The evidence of rapid diffusion of Cu in polycrystalline CdTe due to GB was clearly demonstrated in [15]. Probably the rates of electromigration, which is well manifested for Cu in CdTe are also different for the bulk material and the GB regions. GB are prone to attract and accumulate structural defects and impurities as well as to serve as nuclei for precipitates. It should be mentioned that usually we are not well aware whether these effects are beneficial (e.g. "passivation" of grain boundaries, whatever it means) or detrimental for the cell performance. Anyway, grain boundaries can strongly affect the spatial distribution of the species vital for the cell performance, especially in the fine grain structures like CdTe and CdS thin films. Migration along the GB, especially for fast diffusing species such as Cu, should also lead to their significant redistribution under varying stress conditions and hence may be an important factor in the degradation processes.

The following sections present some of our studies performed at Phase II and aimed at development and checking validity of some approaches we use for studies of basic properties of the cells and their thin film constituents.

2. Deep Traps in CdTe Solar Cells

2.1 Introduction

As mentioned in Sec. 1.4, the problem of detection, identification and studying the properties of deep traps in the cell is an important issue relevant both to the cell performance and to its degradation. Recently we started these studies in collaboration with Dr. R. Ahrenkiel, and Dr. D. Levi (NREL). As in studies presented in the previous section we were interested in comparison of properties of differently processed CdTe/CdS cells. Ahmet Balcioglu (the CSM Ph.D. student advised by Dr. Ahrienkel) was studying the Cu-related deep traps in the CdTe/CdS solar cells fabricated at NREL (CBD CdS, CSS CdTe, and Hg:Cu/graphite back contact) using C-V, C-T, DLTS and ODLTS techniques. Balcioglu's Ph. D. research included similar studies of our cells (CBD CdS, electrodeposited CdTe, and Cu/Au back contact). To date we can compare the results for only the as-prepared cells. Studies of changes caused by stress testing in the CSM cells are intended for Phase III, so that in our Final Report to NREL we will be able to present and analyze differences between the NREL and CSM degraded cells.

2.2 Processing and Characteristics of the Cells Fabricated at CSM

The cells were processed with only small deviations from our standard procedure. The 250 nm thick CdS layer was deposited on commercial tin oxide/glass substrate and annealed with $CdCl_2$ in N_2 for 50 min at 450^{o}C. After electrodepositing ~3 μm thick CdTe, the obtained structure was subjected to $CdCl_2$ treatment in air for 45 min at 410^{o}C. After etching with 0.1% Br_2/methanol, the Cu layers of 30 or 100 Å thickness were thermally evaporated on the CdTe surface followed by annealing at temperatures ranging from 100^o to 250^o C for 15 min in vacuum. Afterwards, a Br_2/methanol etch was applied to remove the remaining Cu from the CdTe surface. Metallization of the back contact was provided by thermal evaporation of gold.

The J-V characteristics of completed cells were measured using an ELH-type tungsten-halogen lamp calibrated with a GaAs standard cell and providing the 1 Sun intensity of light. The results of J-V characterization for the cells prepared with different temperature of the post-Cu annealing are presented in Table 2.1.

Table 2.1 Device performance vs. Cu annealing temperature

Temperature ^{o}C	**Efficiency** %	J_{sc} mA/cm^2	V_{oc} mV	Rs Ω-cm^2	R_{sh} Ω-cm^2	FF %
100	7.00	21.5	670	40.0	230	49
140*	9.00	20.9	732	2.60	475	59
150	10.6	22.8	725	7.00	560	64
170*	8.10	20.4	728	7.70	409	54
200	8.50	22.1	658	9.10	316	59
250	5.30	19.3	564	12.8	190	48

The highest efficiency was demonstrated by the cell with 150°C post-Cu annealing temperature. Efficiency decreases as the annealing temperature goes up or down from 150°C. As to the particular cell parameters (V_{oc}, J_{sc}, etc.), the "150" cell has the highest J_{sc}, R_{sh} and FF values. V_{oc} is only a little lower than that for the neighboring cells, "140*" and "170*" that were processed with 100 Å thick Cu films. These two cells demonstrate considerably lower J_{sc}.

Standard C-V measurements to determine the apparent doping profile were performed at a frequency f=100 kHz using the standard treatment of the data based on the equation [16]:

$$N = \left[\frac{A^2 q \varepsilon \varepsilon_0}{2} \frac{d\left(1/C^2\right)}{dV} \right]^{-1} \qquad (2.1)$$

where C is the measured capacitance, V is the applied bias voltage, A is the area of a cell. The carrier concentration profiles determined for the cells listed in Table 2.1 are shown at Fig. 2.1.

It is to be noted that the "doping level" increases with the annealing temperature and that this level rises at smaller depths, that is closer to the CdS/CdTe interface. For the "150" cell the "doping density" at zero and reverse biases is close to that for the NREL CSS cells, but at the forward biases exceeds those by more than an order of magnitude. The discrepancy for the "200" and "250" cells is remarkably higher.

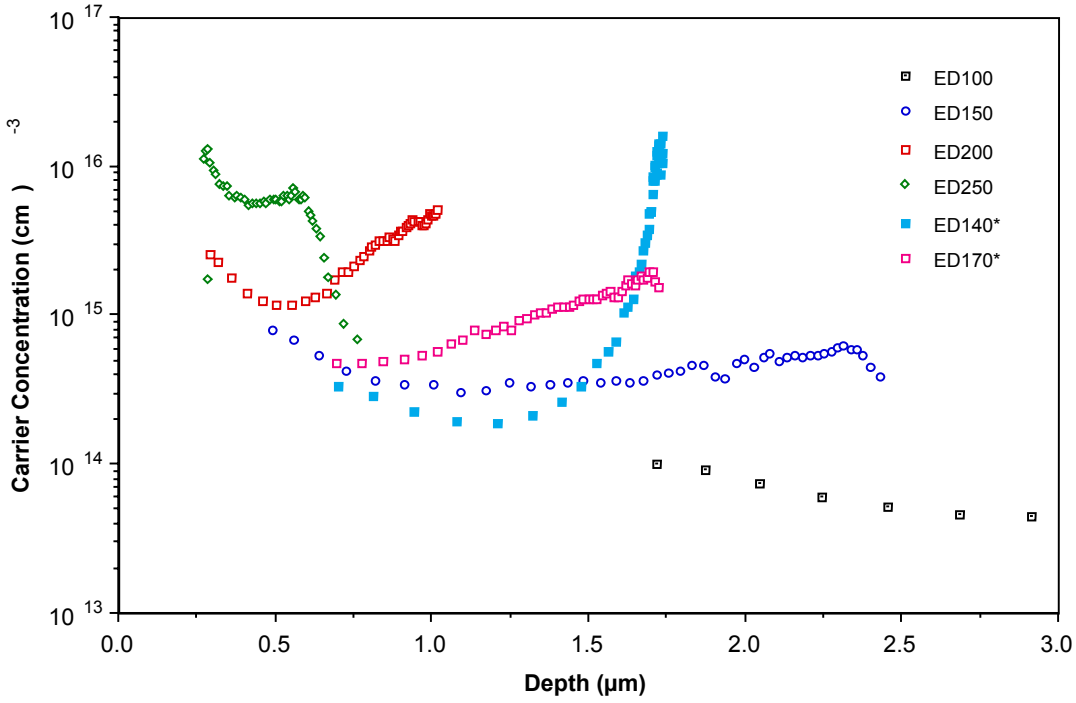

Fig. 2.1 The carrier concentration profile measured at room temperature for various post-Cu annealing temperatures

2.3 C(V, T) and C(V, f) Dependencies

Fig. 2.2 shows the temperature dependence of carrier concentration derived from the C-V measurements for the cell "150". A remarkable decrease is seen as temperature changes from 400 K to 150 K. It should be also mentioned that the capacitance dependence on bias weakens with decreasing temperature. For measurements at 150 K the C value changes by about 5% in the bias range from –1.8V to +0.2V. At T=100 K no change in capacitance could be seen in the same bias range and the depletion width estimated from the capacitance is very close to the CdTe layer thickness. One of probable explanations for this C(T) behavior is carrier freeze-out. If so, one can suppose that the impurity level that provides the dominating contribution to the hole concentration is not shallow, or that it is strongly compensated.

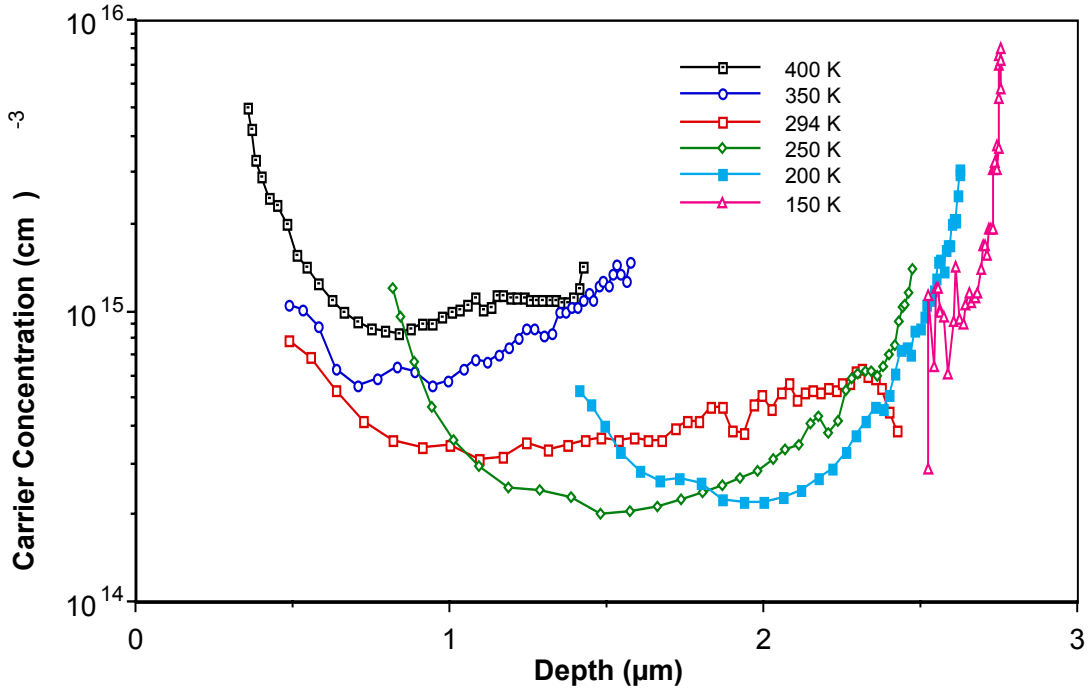

Fig. 2.2 The carrier concentration-depth profile in the cell "150" as a function of temperature

Another possible mechanism of the temperature-dependent capacitance is the influence of deep traps. It is known that in the presence of deep traps two distinct components of the measured capacitance should be considered [16]. The first one is described as the geometry or depletion capacitance, C_d, which is determined by the depletion width and does not depend on the testing voltage frequency, ω (the angular frequency ω [rad/s]=2πf [Hz]). The second component is due to oscillations of the electrical charge trapped by deep levels, named the oscillation capacitance, C_T. The amplitude of these oscillations and hence the magnitude of C_T depends strongly on the relationship between ω and the characteristic frequency of traps, ω_o, which is reciprocal of the characteristic time, τ. For high testing frequencies, $\omega >> \omega_o$, the trapped charge cannot follow

changes of the testing voltage and the C_T value tends to zero. As frequency ω decreases, becoming of the order of ω_o or lower, the C_T value increases and tends to saturation at the level that depends on the trap concentration. Thus the reduction of the measured capacitance with the testing frequency could be considered as an indication of the deep traps presence.

C-V measurements were performed on the cell "150" at room temperature at testing frequencies of 0.1, 1, 10, and 100 kHz. The frequency-dependent capacitance was observed over all the bias range from –2 V to +0.5 V. Reduction of capacitance with frequency was much more pronounced at zero and forward biases than at the reverse bias. Indeed, for V=0 and V=+0.5 v the measured capacitance decreases 2.5 times as frequency rises from 0.1 kHz to 100 kHz, while at V= -2 V the decrease is only of about 25 %. These data show that there exist deep traps in amount comparable to the carrier concentration or even higher, and that the traps are probably distributed non-uniformly over the CdTe thickness.

One more conclusion can be made from these measurements, namely from a rather smooth C(f) dependence. Indeed, the C(f)/C(0.1 kHz) ratio measured at V=0, is equal to 0.7, 0.5 and 0.4 for f=1 kHz, 10 kHz and 100 kHz, respectively. For a single trap level with a certain characteristic frequency ω_o, the $C_T(\omega)$ dependence is described by the equation:

$$C_T(\omega) = C_T(0)\frac{1}{1+(\omega/\omega_o)^2} \qquad (2.2)$$

A significant change in C_T with ω takes place close to ω_o. In the range of $\omega=(1/5\text{-}5)\omega_o$, $C_T(\omega)$ changes from $0.96C_T(0)$ to $0.04C_T(0)$. At lower and higher frequencies the measured capacitance approaches rapidly the saturation levels, $C_0=C_T(0)+C_d$ and $C_\infty=C_d$, respectively. In our measurements C value changed gradually as the testing frequency ω increased by three orders of magnitude. That means that there are several trap levels, possibly spread over some range of energies within the bandgap.

Based on the deep trap concept, we can discuss an alternative explanation for the temperature dependence of capacitance. The characteristic time/frequency of a trap depends on emission rate and varies exponentially with temperature: $\omega_o \propto \exp(-\Delta E/k_B T)$, where ΔE is the distance between the trap level E_T and the edge of the corresponding band, that is $\Delta E=E_T-E_V$ if we consider traps for holes. Thus the traps that are "too slow" at room temperature to follow the oscillating voltage, become "players" when their ω_o approaches ω due to enhanced temperature. It is seen from Eq. 2.2 that contribution of traps to the capacitance measured at some frequency ω, $C_T(\omega)$, increases with rising ω_o, approaching the limiting value $C_T(0)$. The $C_T(0)$ value is determined by the trap concentration, its distribution over the diode thickness, and band bending [16].

While the second mechanism (deep trap contribution) is supported by the data presented above, the first one (increase in carrier concentration with temperature) is also rather probable. It is to be noted that the data presented at Fig. 2.2 were obtained at high frequency of 1 MHz, hence the contribution of deep traps to the total measured capacitance, that is the ratio $C_T/(C_T+C_d)$, was minimized as much as possible. To clarify the role and estimate the individual contributions of these two mechanisms we need to perform more thorough experimental studies and modeling.

We are planning more detailed studies of C(V, f, T) dependencies on the cells with varying Cu content and processing procedures. These measurements will be made in dark and light and hopefully will enable detecting deep traps and studying their characteristics, such as concentration, spatial distribution, energy levels or density of states function, etc. We currently have two LCR meters that cover together the frequency range from 20 Hz to 30 MHz. We are finishing building a chamber for measurements at temperatures above as well as below room temperature. We believe that it would be worthwhile to supplement the C(V, f, T) studies with measurements of the Hall effect (as well as photo-Hall) at different temperatures on the doped and undoped CdTe thin films. The Bio-Rad Hall system we possess provides measurements in the temperature range from about 100 K to 450 K. Recently we have supplied this system with a light source based on the array of the light emitting diodes. Currently we are designing the system that will illuminate the sample with white light using fiber optics.

We have started modeling C-V profiles in the cells with deep traps. The first step was modeling C_d-V profile (high frequency capacitance) for the cells with uniformly distributed acceptors (uniform "doping level"). It was shown that in the trap presence the apparent doping profile, obtained with a common method based on Eq. 2.1, can be rather non-uniform. In particular, it can manifest a sharp increase at high reverse bias voltages. This feature is commonly observed in the cells doped with Cu via the back contact application. Usually it is attributed to the enhanced dopant concentration near the back contact. The non-uniformly distributed traps can also imitate some peaks in the apparent doping profile similar to those observed in the cells stressed at the reverse bias, see Fig. 1.3.

2.4 Deep–Level Transient Spectroscopy (DLTS).

All the DLTS studies were performed at NREL as well as the minority-carrier lifetime and SIMS measurements. The DLTS measurements were used to determine the energy of deep levels in the bandgap and estimate the trap concentration. These measurements were done at a reverse bias of –1.0 V with pulse amplitude of 1V and pulse width of 1.0 ms. The concentration of trap levels was estimated using equation 2.3 [from Ref. 16]:

$$N_T = 2\frac{\Delta C}{C} N\left(\frac{w^2}{(w-\lambda)^2 - (w_o-\lambda)^2}\right) \qquad (2.3)$$

where ΔC, C, $N=(N_A-N_D)$, w, w_o and λ are the DLTS peak maximum, steady state capacitance of a peak maximum, the carrier concentration, the depletion width at reverse bias, depletion width at forward bias, and the edge region. The latter is defined as a distance from the depletion region edge and to the plane where the trap level crosses the Fermi level ("crossing point").

Five deep levels were observed in devices studied in the temperature range of 80 to 450 K. They were designated as E1 (the electron trap), H1, H2, H3, and H4 (all four are the hole traps). Their energies are presented in Table 2.2. It was found that the deep levels were partially annealed as a result of the DLTS scan from 80 to 450 K. The repeated scan revealed reduction of the trap concentration and a significant change in the peak shape. The trap concentrations calculated using the initial DLTS spectra (the first scan 80-450K) are also shown in Table 2.2. The trap

levels H1, H2, and H3 were derived from the DLTS spectra obtained on the partially annealed samples because at the initial scan the DLTS peaks did not shift with the emission rate window. It might be due to the presence of the interfacial layers, non-exponential transients, and large series resistance of a cell.

Table 2.2. The trap levels and concentrations

	Trap level energy				
	E1 E_c-0.37 eV	H1 E_v+0.34 eV	H2 E_v+0.70 eV	H3 E_v+0.70 eV	H4 E_v+0.97 eV
Sample ID (Cu anneal Temperature)	Trap concentration (cm^{-3})				
"100"	$9.7x10^{11}$	-	$5.6x10^{13}$	$7.7x10^{13}$	-
"150"	$3.2x10^{13}$	-	$1.5x10^{14}$	$1.8x10^{14}$	-
"200"	-	$3.5x10^{12}$	$3.0x10^{14}$	$3.9x10^{14}$	$6.5x10^{14}$
"250"	-	$2.5x10^{13}$	-	$5.2x10^{14}$	$1.2x10^{15}$

The estimated concentration of traps is pretty high being comparable to the "doping level" derived from C-V measurements (the free carrier concentration), especially for the deepest H2, H3, and H4 levels. The observed increase in the trap concentration with increasing post-Cu annealing temperature correlates with the increase of Cu concentration in the CdTe indicated by SIMS measurements performed at NREL by Drs. S. Asher and R. Reedy, see Fig. 2.3.

Five deep levels were also revealed in the NREL CSS devices [17, 18] of the level energy : E1*=E_c-0.28eV, H1*=E_V+0.35eV, H2*=E_V+0.45eV, H3*=E_V+0.79eV, and H4*=E_V+0.93eV. These energies are close to those found in the CSM cells except the H2* and H2 levels. Probably the other four levels are associated with the same types of defects in both materials. Small difference in energy for similar states observed in the two materials should not be considered as evidence of a different nature of the defects. Indeed, it could be seen from literature that the estimates in various reports of the levels attributed to the same centers vary depending on the method of the CdTe cell preparation and the CdTe postdeposition treatment. Abou-Elfotouh et. al. [11] observed in the ED-grown CdTe devices a minority carrier trap level with an activation energy of E_c-0.35eV. In as-grown CSS CdTe/CdS cells the E1 level has an activation energy of E_c-0.28 eV [17,18]. After stressing of a cell this level shifts into the band gap by 0.22eV [17]. The H1 level of energy about Ev+0.35 eV was previously reported for the ED-grown,

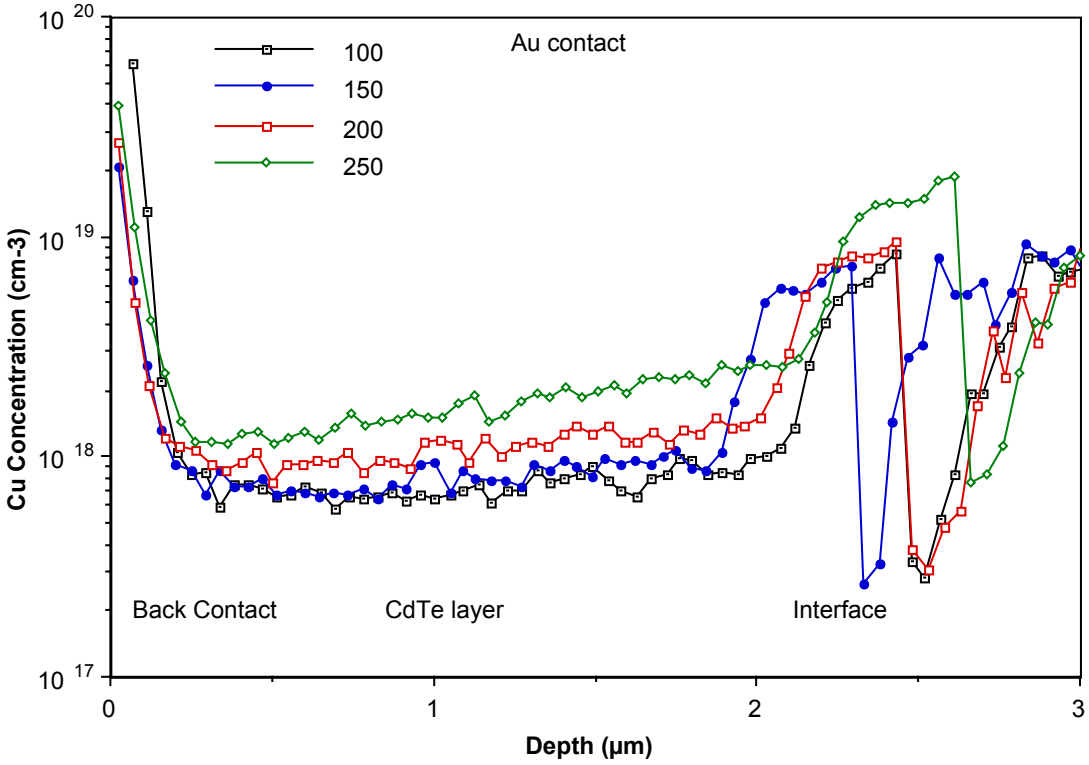

Fig. 2.3 SIMS data on the Cu concentration profile in the CdTe/CdS solar cells with the Cu/Au back contact annealed at different temperatures: 100, 150, 200 and 250^{o} C.

CSS-grown CdTe devices [11, 12, 18, 20, 21] and p-CdTe single crystals [10, 12, 22]. Usually it is attributed to Cu_{Cd} substitution defects. The H3 level with the energy around E_v+0.8eV was reported in numerous publications and is believed to be associated with an acceptor complex involving the native V_{Cd} defect and impurity.

The concentration of levels E1 and H1 are comparable for both the NREL and CSM devices. The concentration of H2 traps was two orders of magnitude higher in the CSM devices. Concentrations of H3 and H4 traps were also significantly higher for the CSM cells.

It is to be noted that for the trap H3 with an activation energy close to the CdTe midgap, the thermal emission rates were found comparable for electrons and holes [23]. This indicates that these traps can act as effective recombination centers. To confirm this, the minority-carrier lifetime was measured in the CSM cells using time-resolved photoluminescence (TRPL). The lifetime was found to depend on the post-Cu annealing temperature and hence the trap concentration. The data presented in Table 2.3 show the tendency of the lifetime to reduce with increasing trap density. The latter increases with the annealing temperature and, as seen from Fig. 2.3, with the Cu content in CdTe.

Table 2.3 Lifetime determined using the TRPL in dependence on the post-Cu annealing temperature

Ann. Temp. (^{o}C)	140	150	170	200	250
Trap conc. (10^{14}cm^{-3})	-	1.8	-	3.9	5.2
Lifetime (ns)	~1.4	~1.3	~1.1	~0.4	~0.2

The minority-carrier lifetime was also measured in the standard NREL CSS devices and was found to be of the order of 0.6-1.0 ns.

2.5 Discussion and Conclusions

The data presented in Sec.2 provide evidence of a few deep levels in the CdTe solar cells doped with Cu. Based on the DLTS studies and especially on the C(f, T) measurements, one can conclude that the concentration of deep electron/hole states is comparable to or even higher than the majority carrier concentration derived from the C-V profiles. Concentration of deep traps depends on the processing technology. In particular, it is different for the NREL CSS cells and the CSM ED cells. For the latter with the Cu/Au back contact the deep trap density increases with the post-Cu annealing temperature, which in turn influences the Cu content in the CdTe detected by SIMS.

There is a significant uncertainty in identity of the defects responsible for the observed deep levels. We could speculate about the nature of a particular center/level based on the literature review, but even these guesses could not be verified unambiguously. The problem of identification is especially complicated for the fine-grain polycrystalline materials. Not all the deep levels reported for the thin film CdTe solar cells have analogs in single crystals. On the other hand, there is evidence of the deep grain boundary states that provide potential barriers for the majority carriers. These states were found in both bicrystals and polycrystalline films, see, e.g., [6, 7, 8]. Probably these GB states are related to the specific GB defects such as dangling bonds. However, one can also suppose an enhanced concentration of impurities, native defects and complexes in the GB region that can provide the level energies different from those in the bulk material because of different environment in the highly disordered GB region.

It is doubtful that the problem of the deep level identity can be solved soon. However, revealing deep traps and their thorough studies on the empirical level are important and urgent issues in the activities aimed at improvement of cell performance and stability. Based on impedance spectroscopy measurements performed in wide frequency and temperature ranges and including bias dependencies, one is able to reveal the presence of deep traps of different kinds and estimate their position in the gap or the density of states function, if they are spread over some energy range. Based on the existent theories with the appropriate modeling we may also extract from

these measurements the emission rate, capture cross-section, concentration and spatial distribution. DLTS, ODLTS, and measurements of lifetime by means of TRPL provide valuable information.

Simultaneously we must establish and explain (using modeling) correlations between the determined trap characteristics, on one hand, and the cell photo-electrical parameters, such as V_{oc}, J_{sc}, R_{se} etc., on the other. We need also to analyze the deep trap influence on the C-V profile and correct the "doping level" profile derived. Finally, the trap characteristics and the cell performance should be related to the cell processing techniques and regimes to provide the basis for optimizing the latter.

3. Near Field Scanning Optical Microscopy (NSOM) of the CdTe/CdS Solar Cells.

3.1 Introduction

To clarify the role of polycrystallinity in forming opto-electronic properties of thin film CdTe/CdS solar cells, it is important to use characterization techniques with a high spatial resolution. Morphological studies (SEM, AFM) of the CdTe absorber layer show that the grain size is usually in a range of one to several microns. Hence we need the tools that provide testing of composition, optical and electronic properties of a material with a spatial resolution on the order of 0.1μm or lower. Along with the scanning tunneling microscopy and spectroscopy, the NSOM is one of the most promising techniques. In our facilities this method and instrumentation were developed by Professor R.T. Collins and Graduate Research Assistant M.K. Herndon. In this section we present some results that demonstrate effectiveness of NSOM for studies and two-dimension mapping of current collection over the cell cross section. One of the major goals of the experiments was to study the interdiffusion of S into CdTe by using the compositional dependence of the ternary $CdTe_{1-x}S_x$ phase band gap and NSOM.

Post growth annealing of the CdTe/CdS films has been shown to enhance the performance of solar cells. Substantial evidence exists that interdiffusion between CdTe and CdS layers occurs during growth and post growth annealing processes [13]. In particular, S diffusion into the CdTe layer leads to the formation of a ternary $CdTe_{1-x}S_x$ phase within the CdTe layer. For S concentrations less than ~25% , bowing in the bandgap of the ternary as a function of x reduces the band gap as S content increases. This leads to a decrease in the low energy cutoff of the device relative to pure CdTe [24]. Various models for the mechanism of S diffusion have been developed, and it is generally believed that grain boundaries must play a role in the diffusion process. This has been difficult, however, to verify experimentally. This study provides evidence that S diffuses preferentially along the grain boundaries in CdTe.

3.2 Experimental Techniques and Procedures

The samples used in these measurements were grown on soda-lime glass coated with a tin oxide TCO. Chemical bath deposition was used to grow a ~200nm thick CdS layer on the SnO_2. CdTe was electrochemically deposited on the CdS layer to a thickness of 3-4 μm. The sample was treated with $CdCl_2$ and annealed at 365^{o}C. Previous work has shown interdiffusion can be observed after the 365°C anneal, and increases significantly with temperature. By 450°C, a nearly uniform S concentration is observed throughout the film [14]. Gold was evaporated through a shadow mask to form a back contact and define individual devices. Capacitance-voltage measurements gave a zero bias depletion width of ~1.5 μm for the diodes and doping level of ~5 x10^{14}/cm^3 in the CdTe.

The glass side of the sample was scribed in the region under a device and broken to expose a cross section of the device. It was mounted so that spatially resolved photocurrent and topographic images of the cross section could be measured with the NSOM. The NSOM is a home built instrument that operates in air. The experiments were done at room temperature. The NSOM probe was made from a single mode optical fiber which was tapered using a micropipette puller and metal-coated, leaving a ~100nm diameter aperture at the tip [25]. The probe was raster scanned across the sample cross section using optically detected shear force feedback to maintain a constant separation of approximately 10nm between the probe tip and sample [26]. Monitoring the feedback signal while raster scanning the sample allowed the topography of the cleaved surface to be measured.

A tunable Ti:Sapphire laser and a 632.8nm HeNe laser were simultaneously coupled into the fiber probe allowing it to be used as an excitation source. Each laser was chopped at a different frequency before being coupled into the fiber. The photocurrent generated in the CdS/CdTe diode was detected for each wavelength using two lock-in amplifiers. The outputs of the lock-in amplifiers were recorded at each point as the sample was scanned. This allowed two spatially-resolved measurements of the generated photocurrent, one for each wavelength of light, to be recorded simultaneously with the surface topography.

Scans of the cell cross section began on the glass side of the junction, and progressed toward the back of the CdTe layer. The same area was scanned several times, each with a different wavelength from the Ti:Sapphire laser, in order to see variations in collection as a function of excitation energy. The HeNe images, taken simultaneously with each Ti:Sapphire measurement, were compared from scan to scan. This reference enabled us to ensure that variations in the Ti:Sapphire measurements were due to changes in excitation wavelength and not due to changes in the probe or scanning conditions.

The band gap of the $CdTe_{1-x}S_x$ ternary phase decreases as a function of x (for $x \leq 0.25$) from ~1.51eV at x=0 to 1.41eV at x=0.25 [27-29]. This dependence of band gap on x allows changes in excitation energy during NSOM measurements to be used to observe spatial variations in the S composition of the $CdTe_{1-x}S_x$ ternary across the heterojunction, and therefore to identify regions of high S content. In the discussion below we have used the bandgap dependence of Ref. 28 to associate optical excitation energies with specific S concentrations. In general, however, the band edge of polycrystalline films shows inhomogeneous broadening due to effects such as strain, defects, and alloying, which can lead to an apparent bandgap which is lower than that for crystalline material. Because of this broadening and the uncertainties in the reported composition dependence of the $CdTe_{1-x}S_x$ band gap, relative changes and spatial variations in S composition found from optical measurements are likely to be much more reliable than the numerical S compositions inferred from the measurements. The later should probably be viewed as correct to within a few percent.

3.3 Experimental Results and Discussion

Figure 3.1 shows a topographic image and three photocurrent images, each produced using a different excitation energy. The images are 4.8 x 4.8 μm. The topography measurements showed

an average grain size of 1-2 μm. A small amount of drift occurred between scans. Comparison of the locations of individual grains seen in the topographic images allows us to track this drift. The layers present in the film have been identified adjacent to Figs. 3.1a and 3.1b. The interface between the glass and film is evident as the horizontal feature across the bottom of the topography image. One obvious grain, which will be discussed in more detail below, has been outlined on the topography plot (Fig. 3.1(a)). The topography measurements obtained in registry with each photocurrent measurement were used to locate this feature in subsequent scans, allowing this region to be identified in the photocurrent images in Figs. 3.1(b)-3.1(d).

For 1.615 eV excitation (Fig.3.1(b)), which is a little more than 100 meV above the CdTe bandgap, we see the photocurrent is strongly peaked near the junction, and decreases toward the back of the device. This is typical of measurements at energies above bandgap. In general, the photocurrent becomes even more strongly peaked near the CdTe/CdS junction as energy increases. As energy decreases below the CdTe bandgap to 1.463eV (Fig. 3.1(c)), corresponding to a S composition of 6%, the collection efficiency at the back of the device improves relative to that at the interface. We have observed this effect (a widening of the collection region at longer wavelength) in most edge cleaved semiconductor diodes we have studied. We attribute it to a competition between surface recombination and collection by the junction. At longer wavelengths, the light is absorbed further from the surface, allowing more of the carriers to be collected by the junction before recombining at the surface. Similar observations and conclusions were presented in Ref. 30. We note that the carrier collection region at this energy extends from the junction to the back of the device and that the average collection efficiency at the junction and near the back are roughly the same. Simplistically, the width of the collection region is determined by the depletion width and the minority carrier diffusion length. Since our depletion width is ~1.5μm, this indicates a minority carrier diffusion length of more than 2μm.

At 1.422eV (Fig.3.1(d)), the excitation energy is 80meV below the CdTe band gap and corresponds to a S content of 16%. Here the width of the collection region has once again decreased. This is the result of carriers being generated mainly in the higher S content, lower bandgap, $CdTe_{1-x}S_x$ ternary phase, which is most likely to exist close to the CdS/CdTe junction. The S concentration we would infer near the junction in Fig.3.1(d) is larger than the reported immiscibility gap composition of ~6% at 415°C [13]. This may in part be due to the uncertainties in quantifying S concentration mentioned above.

For excitation energies below the CdTe band gap, a large amount of contrast was visible across the photocurrent images. For example, localized regions of higher photocurrent are visible near the interface in both Figs. 3.1(c) and 3.1(d). Presumably this contrast arises from variation in S content and hence bandgap across these regions. A particularly interesting example of this contrast is seen in Fig. 3.1(c) where a loop of higher photocurrent is clearly visible within the outlined region. This correlates exactly with the boundary of the grain identified in Fig. 3.1(a). To clarify the energy dependence of this feature, a series of measurements across this grain was recorded while varying the excitation energy from 30meV above to 60meV below the CdTe band gap. The results are shown in Fig. 3.2 where each line on the graph represents a single horizontal scan across the grain. Each scan was made at the same location using a different excitation energy.

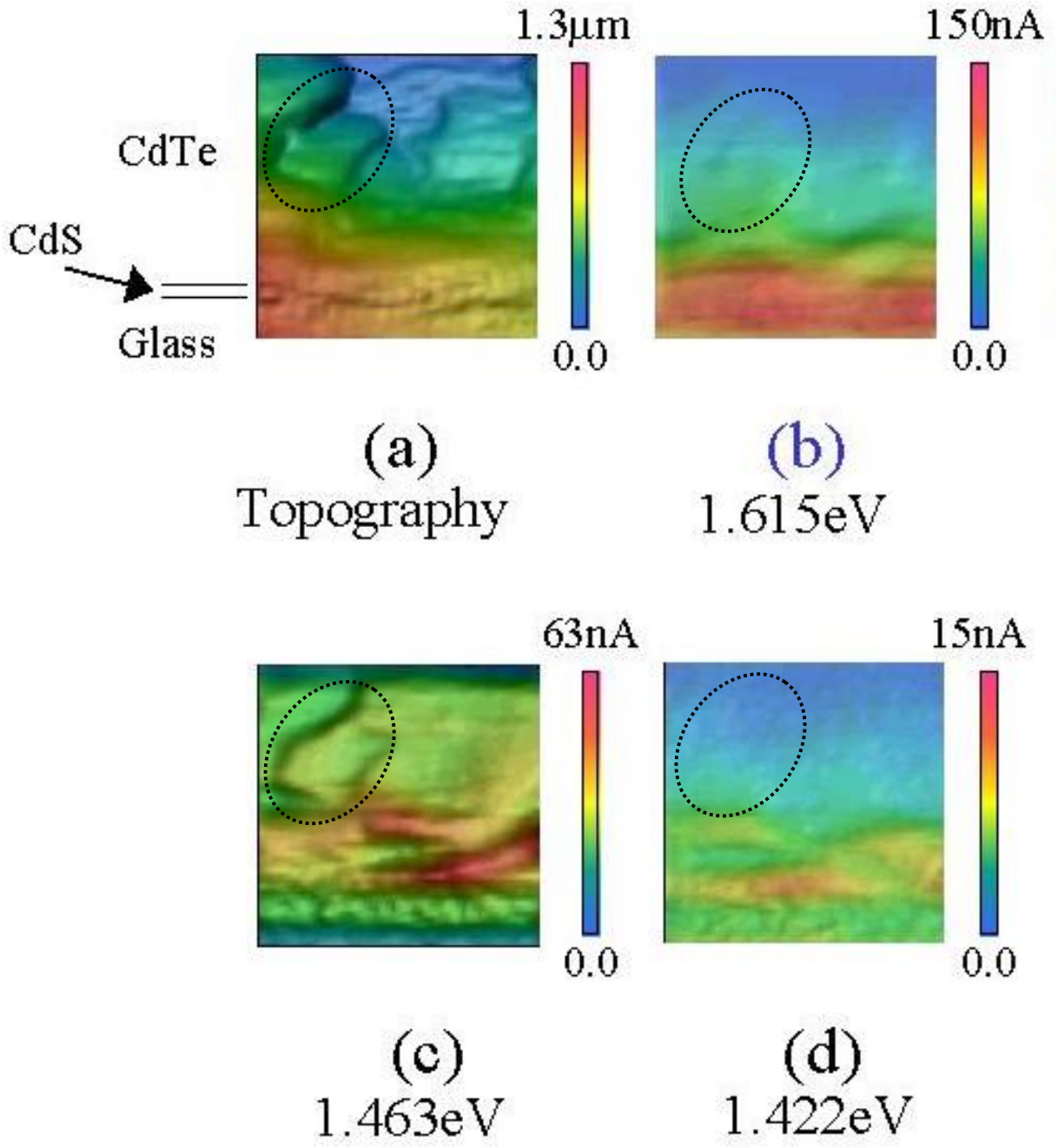

Fig. 3.1. Topography (a) and photocurrent (b-d) NSOM measurements taken on the cross section of a CdS/CdTe solar cell. The same grain has been outlined in the topography and in each of the photocurrent images. The shift in its position is due to drift which was tracked using the topographic images. (b) The excitation energy of 1.615eV is above the CdTe bandgap. (c) The excitation energy of 1.463eV is ~50 meV below the CdTe bandgap. Increased width of the collection region in the CdTe layer is observed compared to (b). For the marked grain, the collection is much greater at the boundary than in the interior. (d) The excitation energy is 1.422eV.

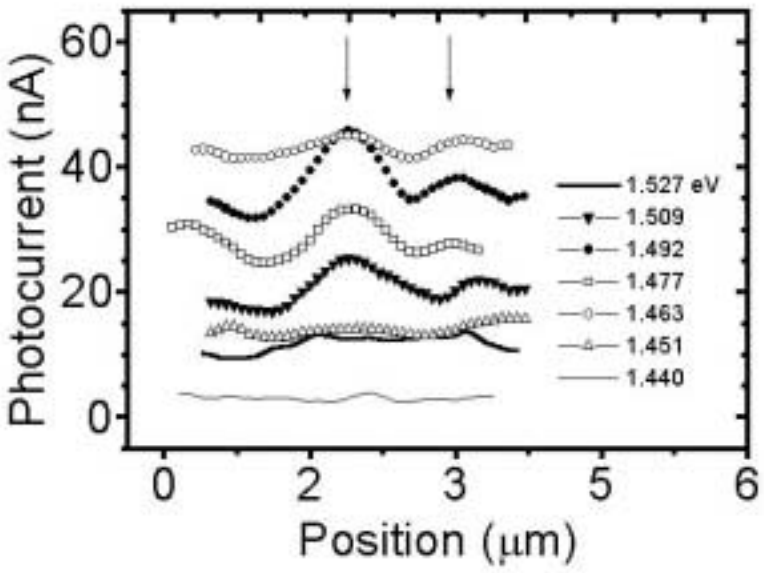

Fig. 3.2. The plot showing line traces taken from single scans across the grain outlined in Figure 3.1. The arrows indicate the location of the grain boundaries. Increased collection at the boundaries relative to the interior of the grain is observed in the scans taken at or just below the CdTe band gap. This indicates that the boundary has a lower energy gap, and therefore higher S composition, than the grain center.

In agreement with the data in Fig. 3.1, as energy decreases, the traces in Fig. 3.2 initially show an overall increase in the average value of the photocurrent, that is maximum for energies just below the CdTe bandgap. As excitation energy decreases further, the average value of the photocurrent drops. Nearly all the signal has disappeared in the 1.44eV scan.

Comparison with topographic data shows that the two peaks in the line traces, which are indicated by arrows in Fig. 3.2, occur at the grain boundary. The relative peak height, or contrast, is largest at 1.492 eV. The region around the boundaries collects less relative to the boundaries as the excitation energy falls below the CdTe band gap. This is presumably due to the boundary material having a lower band gap, and therefore higher S concentration, than the grain center. The contrast first becomes visible at 1.509 eV and finally disappears at 1.451 eV, allowing us to estimate that the region away from the grain boundary is nearly pure CdTe while at the boundary the S concentration is ~ 8%.

In the discussion above, we have attributed features in the photocurrent images to spatial variations in absorption which arise from changes in bandgap across polycrystalline grains due to the presence of $CdTe_xS_{1-x}$. Contrast can also originate from other sources including coupling between topography and photocurrent, and spatial variations in the collection efficiency of carriers created by the NSOM. We were able to discount the possibility that the enhanced collection was somehow due to topography affecting the coupling of light into the sample, since

many such grain boundaries did not show a significant variation in photocurrent. This can be seen in Fig. 3.1 where several grain boundaries visible in the topography do not show large photocurrent contrast. Our tests also showed that the enhanced contrast at the boundaries was independent of such measurement parameters as probe-sample separation, illumination intensity, and scan speed.

The presence of spatial variations in the efficiency with which carriers are collected is a more interesting possibility to consider. For the photocurrent measurements shown in Figs. 3.1 and 3.2, small changes in excitation energy dramatically affect the spatial nonuniformities observed. This leads us to conclude that they are not due to variations in collection efficiency, as we would expect such variations to be observable over a broader range of wavelengths. In some cross sectional photocurrent images of these devices we have, however, observed enhancements in photocurrent near grain boundaries which are present not only at energies below the CdTe bandgap but also well above the bandgap, and which we believe are due to enhanced collection efficiency near the grain boundary. Probably, this effect is not due to (or not only to) the presence of the ternary phase at the GB region. In any case the effect deserves to be studied more thoroughly.

3.4 Conclusions

- Experimental results presented in this report demonstrate the effectiveness of NSOM as a high resolution method for studies and two dimensional mapping of current collection over the cell cross section.

- Variation of excitation wavelength from above to below CdTe bandgap provide new options for correlating specific topographic features of carrier photogeneration and current collection in polycrystalline thin film solar cells.

- The S concentration across annealed CdTe/CdS heterojunctions is quite nonuniform. We were able to directly observe regions at grain boundaries which have a lower band gap than that at grain centers, indicating a higher S content at the boundary. This provides very strong evidence that S diffuses preferentially along the grain boundaries of polycrystalline CdTe and suggests that the overall lack of uniformity in S composition is a result of this grain boundary assisted diffusion mechanism.

- In some cross sectional photocurrent images, enhancements were observed in photocurrent near grain boundaries which are present from energies well above the CdTe bandgap to below the gap and which we believe are due to enhanced collection efficiency near the grain boundary. This result is of a significant importance if verified by future studies. Exploration of transport effects near grain boundaries in more detail hopefully can clarify mechanisms of grain boundary effect on cell performance.

We thankfully acknowledge support from the National Science Foundation under Grant No. DMR-9704780.

4. Impedance Spectroscopy of CdTe Thin Films

4.1 Introduction

Measurements of the complex impedance on polycrystalline films in a wide frequency range (impedance spectroscopy) are aimed at studies of electronic properties of grain boundaries (GB). They represent a technical approach to the problem of polycrystallinity different from that used in the previous section. While NSOM is a high spatial resolution technique that allows testing properties of individual grains and GB's, the impedance spectroscopy measurements characterize properties of a film as a whole. Then, based on some physical and electrical models we extract from these measurements the parameters averaged over numerous grain boundaries in a sample. The validity of the models used must always be considered. We need to analyze conditions under which the particular models are valid or at least provide reasonably small errors in the parameter estimates derived from the measurements.

In this section we present and discuss:
- physical and electrical models we use;
- issues related to the experimental techniques and procedures;
- some results obtained on differently processed CdTe thin films.

4.2 Physical and Electrical Models

The basic idea of the method is that a polycrystalline film consists of two phases with very distinct electrical properties. One phase is the intragrain (IG) material and the other is represented by the GB regions with the potential barriers for the majority carriers. GB is characterized by high resistance and also by capacitance provided by depleted semi-insulating layers adjacent to the GB. The grain is assumed to be electrically equivalent to a resistor, R_{IG}, whereas the GB is electrically modeled as a resistor, R_{GB}, in parallel with a capacitor, C_{GB}, see Fig. 4.1.

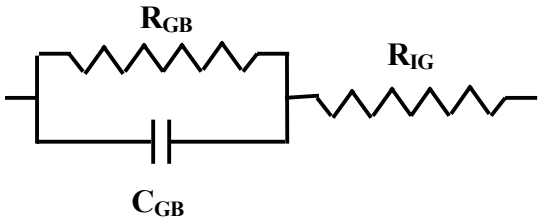

Fig.4.1 The simplest electrical model of a polycrystalline film.Resistor R_{GB} and capacitor C_{GB} represent grain boundary. Resistor R_{IG} represents the intragrain material.

At low frequencies the film impedance is almost totally defined by the GB resistance. At high frequencies the GB capacitor effectively shunts the GB resistor, so that the measured resistance tends to the IG resistance. Thus measurements in a wide frequency range provide an opportunity

to separate individual contributions of GB and IG material to the sample resistance and determine the GB capacitance.

The LCR meter can display the results of measurements in various modes. We use most commonly the "p"-mode which suggests the tested circuit composed of a resistor and capacitor in parallel, and the "s"-mode which suggests the circuit composed of a resistor and capacitor in series. Thus we analyze simultaneously the measured frequency dependencies of R_p, C_p, R_s and C_s. For the film model in Fig. 4.1, the relations between the displayed R_p, C_p, R_s and C_s values, and the sample parameters, R_{GB}, C_{GB}, and R_{IG} are as follows:

$$R_p=R_{IG}+[R_{GB}/(1+\alpha)]\cdot\{1+\alpha/[1+(R_{IG}/R_{GB})(1+\alpha)]\} \quad (4.1)$$

$$R_s=R_{IG}+R_{GB}/(1+\alpha) \quad (4.2)$$

$$C_p=C_{GB}\cdot(1+\alpha)/\{[1+R_{IG}/R_{GB}(1+\alpha)]^2+\alpha\} \quad (4.3)$$

$$C_s=C\cdot(1+\alpha)/\alpha \quad (4.4)$$

where $\alpha=(R_{GB}C_{GB}\omega)^2$ and ω is the angular frequency.

Fig. 4.2 shows that the dependencies calculated with Eqs. 4.1 – 4.4 fit good measured frequency dependencies of R_p and R_s. Good fitting was also demonstrated for C_p and C_s. In reality, the equivalent circuit of any polycrystalline sample should consist of numerous blocks like that at Fig. 4.1 connected in parallel and in series. Good fitting means that using a single block model and "lumped" parameters is an acceptable procedure for these measurements, and a single block may represent adequately a polycrystalline sample composed of a lot of grains. The fitted results make it possible to extract lumped parameters, R_{GB}, C_{GB} and R_{IG} from the measurements. Incorporating more than one block yielded even better fits, which gives a simple means for evaluating the range of distribution of these parameters. Very good fitting was found when three blocks were incorporated with the same C_{GB} and R_{IG} values while R_{GB} values for the three blocks related to each other as 1:1.5:2. Since resistance of the GB depends exponentially on the barrier height, it may be concluded that standard deviation of the latter from the average is very small.

The method was recently proved to be effective for studies of grain boundaries in CdTe and CdS thin films on insulating substrates [31, 7, 8, 32]. But it should be mentioned that application of the method is limited to the films with high resistance grain boundaries. As seen from Eqs. 4.1 and 4.2, an effective shunting of the resistor R_{GB} by the capacitor C_{GB} takes place under condition: $\alpha=(R_{GB}C_{GB}\omega)^2>1$, that is when the characteristic frequency $\omega_{GB}=(R_{GB}C_{GB})^{-1}$ is smaller than the testing voltage frequency, ω.

In general, the real physical and hence electrical models should be more complex than those considered above. For example, as seen from the data in Sec. 2, the grain bulk contains deep traps that contribute to the capacitance measured on the cells ("oscillating capacitance"). In general, these traps also may contribute to the capacitance of the films on the insulating substrates that we study with the impedance spectroscopy. This "oscillating" capacitance is connected in parallel to the IG resistance and may shunt it, leading to underestimation of R_{IG} and overestimation of the GB capacitance.

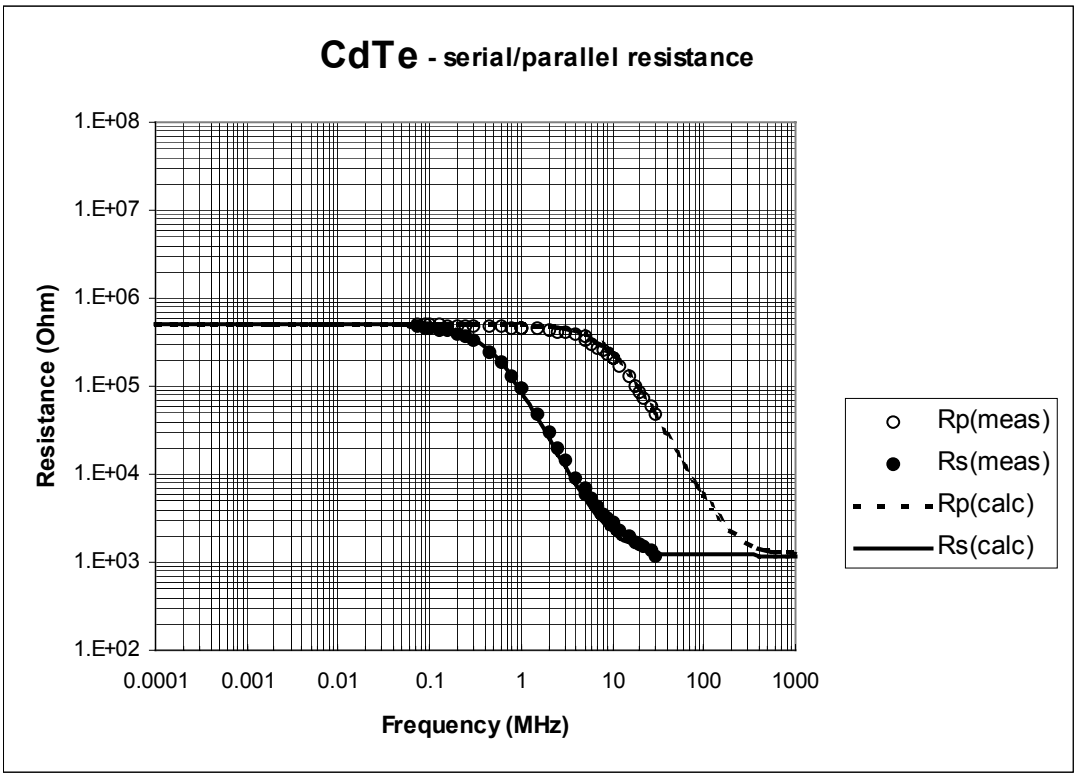

Fig. 4.2 Experimental results for the resistance of a CdTe layer demonstrating the fit to a simple one-block equivalent circuit

Fig. 4.3 presents the electrical model for this case. For the films we have studied so far, $R_{IG}<<R_{GB}$, and, according to our estimates, C_{IG} does not exceed significantly C_{GB}. That means that at not too high frequencies the total measured impedance is dominated by grain boundaries. Only in the range of frequency above 10 MHz we could see some small deviations of the measured parameters from those calculated with equations 4.1-4.4 that might be attributed to the influence of C_{IG}. It could be thought that our pervious estimates of R_{IG} based on the simple model (Fig. 4.1) are not too accurate. As to the GB parameters obtained by fitting experimental and calculated data in the frequency range below 5-10 MHz, we believe they are reliable.

Recently we measured undoped CdTe films on bare glass substrates that demonstrate the Hall concentration of holes at room temperature near $10^{11}cm^{-3}$ and Hall mobility in a range of 5-20 cm^2/Vs. The latter value indicates that the GB resistance is not high, probably being comparable to the IG resistance. For films of this kind we will have to use the model of Fig. 4.3 to analyze the impedance spectroscopy data. It is unclear as yet whether we will be able to separate and estimate accurately the GB and IG resistance and capacitance.

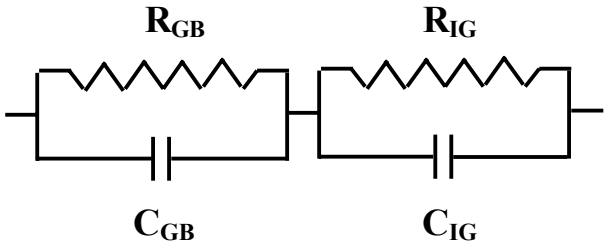

Fig. 4.3 Electrical model that includes capacitance of the intragrain material.

We have also found [32, 8] that the measured capacitance changes with the bias applied to the sample. As bias deviates from zero, capacitance increases and tends to saturation, and then decreases as bias voltage increases further. The bias-dependent resistance and capacitance were observed previously on a variety of semiconductors containing grain boundaries, e.g. on Si [33], Ge [34], GaAs [35] and CdTe bicrystals [6], and ZnO varistors [36]. The non-linearity of the DC resistance was explained and modeled in [37] based on the idea that under high enough bias the electrical charge trapped by the GB states and the GB potential barrier height increase. This in turn should lead to increase in the GB depletion width and reduce of the measured depletion capacitance. This effect was observed and discussed in [6, 35].

However a significant increase under bias applied was observed in the low-frequency range on Si bicrystals [38]. This effect was attributed to the carrier transfer between the grain and the GB traps which is out of phase with the oscillating testing voltage. Thus the total AC current is a sum of grain-to-grain and grain-to-GB currents. Accordingly, the electrical model of a grain boundary should be modified (see Fig. 4.4). The out-of-phase grain-to-GB carrier transport can be modeled with a capacitor C_T in series with a resistor R_T, which represents a finite probability for carriers incident on the GB to be trapped. The product $R_TC_T \equiv \tau_T = 1/\omega_T$ is the characteristic time of a trap (reciprocal of the characteristic frequency ω_T) and is related to the emission rate. The in-phase and out-of-phase grain-to-grain transports are modeled with a resistor $R_{G\text{-}G}$ and a capacitor $C_{G\text{-}G}$. Capacitors C_T and $C_{G\text{-}G}$ represent the oscillating and depletion capacitances of the GB, respectively.

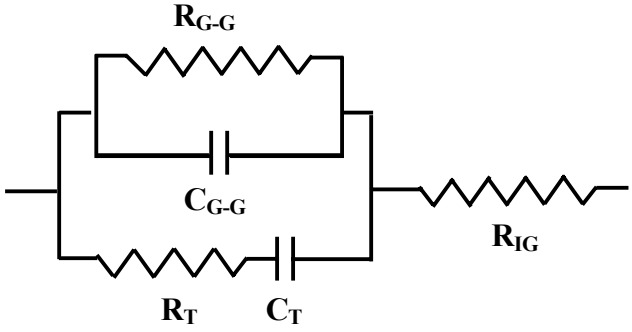

Fig. 4.4. Modified electrical model for the polycrystalline film. $R_{G\text{-}G}$ and $C_{G\text{-}G}$ relate to the grain-to-grain electrical transport, R_T and C_T to the grain-to-GB transport; R_{IG} represents resistance of the intragrain material.

When fitting our AC measurements of CdTe films with this electrical model, it was found that R_{IG} is orders of magnitude smaller than R_{G-G} and R_T. Its variation in reasonable limits does not influence the fitting value of capacitance, at least in the frequency range of f<5MHz. If we neglect R_{IG}, the capacitance value measured in "p" mode is described by equation:

$$C_p=C_{G-G}+C_T/[1+(R_TC_T\omega)^2]= C_{G-G}+C_T/[1+(\omega/\omega_T)^2] \quad (4.5)$$

It is seen that for the given R_T and C_T values, the contribution of the oscillating component to the total measured capacitance decreases as the frequency increases, which allows us to separate C_{G-G} and C_T. This result is in agreement with our experimental data and also consistent with observations and discussion in [38,39]. The contribution of C_T also decreases with increase in R_T (decrease in ω_T). It was found that illumination of the sample diminishes R_T which makes the capacitance dependence on bias voltage more pronounced and easier to measure.

4.3 Experimental Technical Problems of Measurement.

4.3.1 Samples for AC characterization.

The samples for measurement are semiconductor films on insulating substrates such as glass. The sample impedance is measured in plane with a two-electrode method. Parallel metal strips are evaporated on the surface of the semiconductor film through the mask. To provide semi-ohmic low-resistance contacts we evaporate gold on CdTe and aluminum on CdS. DC J-V characteristics measured are linear, indicating ohmic contacts. On the surface of each sample we normally evaporate six metal strips for the reasons discussed below.

LCR meters have limitations on the resistance of the tested sample. A Hewlett-Packard LCR meter, Model 4285, we have been using so far, is capable to measure and display the results if the sample resistance (real part of the impedance) does not exceed ~50 MΩ. The DC sheet resistance of the CdTe and CdS films we have measured varied in a wide range up to tens and hundreds GΩ. With increasing frequency the real part of impedance reduces (see Eqs. 4.1 and 4.2) and becomes measurable at some high enough frequency. But this narrows the frequency range we can analyze and make estimates of the film parameters (R_{GB}, C_{GB}, etc.) less accurate and reliable. To decrease the sample resistance, that is the film resistance between two neighboring metal strips, we use the geometry factor. The mask we use provides the distance between metal electrodes of 0.18mm, while the sample width (the size perpendicular to the current direction) is usually of 20 mm. This geometry reduced the sample resistance by more than two orders of magnitude as compared to the square-shaped sample. By depositing several strips on the semiconductor surface, we produce several identical samples, e.g., five samples between six metal strips. When connecting the samples in parallel, we decrease the resistance by a factor of five.

Parallel connection of the individual samples increases the capacitance to be measured. This is an additional advantage of multiple metal strips. The single sample capacitance is rather small, usually ~1 pF. For such a small capacitance to be measured, the problem of parasitic capacitance and inductance becomes important. Even the "leads zeroing" procedure provided by the LCR meter does not necessarily ensure exclusion of the parasitic effects. The multi-strip geometry

helped us to some extent to estimate possible inaccuracy due to the parasitic elements in the measurement circuit. First, the capacitance was measured on all the individual samples on the same film, that is capacitance values between neighboring pares of strips. Then the same measurements were performed on the samples connected in parallel. Based on individual capacitance values we calculated the expected capacitance of two, three, four or five samples in parallel and compared these values with the measured ones. Discrepancy was usually small, not higher than 5%. We consider this result as some (if not the ultimate) verification of the small influence of parasitic reactant elements. Another way to estimate parasitic effects we used was to measure the glass substrate with electrodes but without semiconductor film. It was found that the measured capacitance (imaginary part of admittance) was by two orders lower than that measured with the semiconductor film.

4.3.2 Measurements in dark and light.

The sample to be characterized is positioned in a metal box whose internal and external surfaces are coated with a black paint. The sample can be illuminated through a glass window in the top cover of the box. We use a white light source for illumination and neutral filters to vary the light intensity. To provide dark-measurement conditions the box is thoroughly protected from the room light with a multi-layer dense black cloth.

All the CdTe and CdS polycrystalline films manifest a significant photo-conductivity effect, especially films with very high GB resistance. Even illumination with a light of 0.1 Sun intensity provides a 1000 fold decrease in measured resistance for some films. Usually a significant difference is also observed between resistances measured without using a light source but with and without the black cloth. The measured capacitance is also sensitive to the illumination, especially the bias dependent capacitances.

Another issue to be discussed is the kinetics of photo-response. After turning light on, a steady state resistance value is achieved in a short time not exceeding one or several seconds. After switching the light off, a rapid increase in resistance takes place initially, followed by very slow restoration of the "dark" resistance. This process is not a simple exponential decay. The instantaneous relaxation time increases with real time of observation, so that we may wait for hours or sometimes days for the total restoration of the dark resistance. Thus the real "dark" conditions are not achievable in a reasonable time. It is beyond any doubt that thorough studies of transient effects are of great interest themselves. These studies can shed light on some important properties of deep GB electron states. They also might clarify some light-induced changes in defects accumulated at the GB region and their spatial distribution. However, influence of transient effects, which are different for different films, should be eliminated as much as possible when we are aimed at routine comparative studies of numerous differently processed and stressed films. In this case we have to give up the dark measurements and confine ourselves to the measurements under controllable light conditions. It was found that the 0.1 Sun light intensity is usually sufficient for these measurements. First, at this light intensity no long-term transient effects in films were observed at room temperature. Then, the film resistance under these conditions reduces, making possible the AC measurements in the whole frequency range (see. Sec. 4.2.1). At last, but not least, the sample heating by light is small, which is

important when studying the GB resistance, which depends exponentially on temperature due to the GB potential barriers.

4.4 Impedance Spectroscopy Studies of CdTe Films.

Here we present the comparative studies of the films with different post-deposition treatments. These studies are continued and their final results will be presented and discussed in more detail later. CdTe films on the glass substrates were prepared by B. McCandless at the Institute of Energy Conversion (University of Delaware) with physical vapor deposition at a substrate temperature of 325^o C. Some films were treated with $CdCl_2$ and doped with S or Cu at the CSM facilities. AC measurements of R_p, R_s, C_p, and C_s were performed with and without illumination. Measurements at zero bias and fitting data with Eqs. 4.1- 4.4 were used to obtain R_{GB}, C_{GB}, and R_{IG} values for each sample.

The R_{GB} value was orders of magnitude greater than the R_{IG} for all films. The estimated potential barrier height Φ_b without illumination varied from 0.7 to 0.3 eV depending on post-deposition treatment. The decrease in barrier height caused by illumination achieved for some films 0.15-0.2eV. The $CdCl_2$ treatment lowered R_{GB} under illumination only. Sulfur diffusion lowered R_{GB} under illumination, but increased R_{GB} when in "dark". Finally, copper diffusion into CdTe films was found to lower R_{GB} both in "dark" and under illumination by more than two orders of magnitude.

As mentioned in Sec. 4.2, the contribution of oscillating capacitance is zero without application of bias. Thus capacitance measured at zero bias is equal to the depletion capacitance. Based on the average grain size and film geometry and assuming the square-shaped grains of the same size, we estimated the specific GB depletion capacitance $C_{G\text{-}G}$*, that is capacitance per unit area of a single GB. Its value did not vary much with the varying post deposition treatment and was in a range of around $5x10^{-7}$ F/cm^2. The space charge density N_{GB} in the GB depletion region was estimated from the $C_{G\text{-}G}$* value using the equation:

$$N_{GB}=(8\Phi_{b0}/e\varepsilon\varepsilon_o)(C_{G\text{-}G}^*)^2 \qquad (4.6)$$

where Φ_{b0} is the zero-bias potential barrier height. The obtained value was in the range of 10^{18}cm^{-3}. The $C_{G\text{-}G}$*, hence the N_{GB} value might be overestimated by assuming such a simple morphology of the films but the error could not be orders of magnitude. Thus one can conclude that N_{GB} is much higher than the carrier concentration derived from the C-V measurements on the CdTe cells. This result is consistent with the estimates obtained in [7] by using essentially different method. As mentioned in Sec.1.4, in the case of dominating compensation of acceptors by the GB states, the negative space charge density in the GB proximity, should be close to N_A and can be much higher than the free hole concentration derived from the C-V profile. However, one cannot exclude an enhanced doping density in the GB region due to accumulation of dopant. Indeed, the estimated value of N_{GB} for the Cu-doped films was several times higher than that for the undoped films.

As shown in [38], measurements of bias-dependent oscillating capacitance C_T can provide an estimate of the GB density of states. In [32] we have presented a simplified analysis of the problem limited to the case of a low bias applied to a single GB, namely, $V^*<\Phi_{b0}/2$. For the specific capacitance we have obtained the equation:

$$C_T^*=\{2C_{G\text{-}G}^*(0)/[1+4C_{G\text{-}G}^*(0)/e^2N_T]\}\times \tanh\,(V^*/2kT) \qquad (4.7)$$

where $V^*=V_{bias}d/l$, V_{bias} is the bias voltage applied between probes, l is the inter-probe distance, and d is an average grain size. The density of the GB traps, N_T, is assumed constant, because a small V* effects both the trap occupation and Fermi level position with respect to the trap band only slightly.

Thus the measured capacitance increases with bias until it reaches saturation at $V^*>2k_BT$, then it may slowly decrease due to the geometry capacitance. Using this model, and allowing d and N_T to be fitting parameters, one can obtain information about average grain size and GB density of states:

$$N_T = (4/e^2)\times \beta/(2-\beta)\times C_{G\text{-}G}^*(0);\ \ \beta= C_T^{sat}/C_{G\text{-}G}(0) \qquad (4.8)$$

It was found that the measured $C_T(V_{bias})$ dependence fits the equation above for all the films studied. The estimated density of the GB states, N_T, was in the range of 10^{12} to 10^{13}cm^2. For Cu-doped films it was higher than for the undoped ones.

5. Studies of Band Spectrum and Electron Scattering in Transparent Conducting Oxides

5.1 Introduction

To improve the properties of existing and new TCOs, it is important to put the topic on a solid scientific basis by obtaining detailed information about the electronic properties of thin films, as well as about the effect of substrates (glass, polymer, other semiconductors etc.), film structure, morphology etc. This information, and its theoretical analysis, will enable an estimate to be made of the limiting mobility and of the achievable figure-of-merit for practical TCOs. The approach requires a variety of methods and tools for characterization of the fabricated samples as well as solid scientific grounds for interpretation and theoretical analysis of the data.

In our previous Annual Report to NREL [32] we presented studies of band parameters and electron scattering in SnO_2:F thin films. It was shown that worthwhile information and reliable numerical estimates of the parameters can be obtained by means of optical characterization (ellipsometry), the Hall and Seebeck coefficients measurements. In this report we present a technique named the four-coefficient (FC) method based on studying electron transport phenomena in stationary external fields. This method is aimed at determination of mobility, the density-of-states (DOS) effective mass, m_d*, and scattering parameter, r (hence the dominating scattering mechanism) as a function of the carrier concentration/Fermi level position. It is based on the simultaneous measurements of four transport coefficients: electrical conductivity, σ, the Hall, Seebeck, and Nernst-Ettingshausen coefficients, R_H, α, and Q, respectively. The method does not require fulfilling the condition of strong magnetic field (μB>>1) as some powerful methods (e.g. cyclotron resonance, Shubnikov-de Haas and de Haas- van Alphen effects) for the band structure studies do. This is a significant advantage for TCOs that typically have small mobilities and do not meet this condition (μ < 100 cm^2 V^{-1} s^{-1}, and μB <0.01 for B = 1 Tesla). Measurements in a wide range of carrier concentration/Fermi level position provide detection of non-parabolicity and establishment of real dependence of the electron energy on the wave vector, $E(\boldsymbol{k})$. Being combined with measurements of the plasma and collision frequencies (ultra-high frequency electron transport) the FC method provides guidance about the shape of the constant-energy surfaces in $\boldsymbol{k}$-space. This combination also allows an elucidation of the influence of the grain boundaries on electrical properties and, in particular, on the measured film sheet resistance and bulk resistivity.

The method was first proposed and applied to studies of n-PbTe in [40] and then used widely for studying a variety of semiconductors and semimetals, in both bulk and thin film form, see, e.g., [41-43]. In 1995 joint studies by Dr. T. Coutts, NREL and Dr. V. Kaydanov, CSM were started, aimed at applying the method to investigation of TCO materials. It is hard to overestimate the contribution of W. Mulligan and D. Young to these studies. Both were CSM Ph.D. students advised by T. Coutts and V. Kaydanov. Dr. Mulligan created the first system that provided measurements of the four coefficients in typical TCO thin films and performed preliminary experiments on cadmium stannate [44]. Dr. Young has developed new, more perfect and sophisticated measurement equipment and performed systematic comparative studies of a variety of TCO thin polycrystalline film materials [45-48].

In section 5.2 we discuss the electronic properties that determine carrier mobility and affect the optical transmittance. These are primarily the effective mass tensor and the nature of carrier scattering processes. In section 5.3 we describe and ground theoretically the four-coefficient method. The next section 5.4 shows what information and in what way could be extracted from the comparison the stationary-field and ultra-high frequency (optical) data. Section 5.5 presents the major results of the TCO thin film studies by using the methods described in previous sections.

5.2 Electron Parameters to be Determined. Their Influence on the TCO Figure-of-Merit.

5.2.1 Band model, the effective mass tensor, and density of states.

Along with the bandgap that defines the short-wavelength transmission limit of the material, other details of the band structure are necessary to determine the achievable figure-of-merit. In general, we need to know the dependence of the carrier energy on its wave vector, $\boldsymbol{k}$, in the conduction band. In particular, we are interested in the shape of the constant-energy surfaces in $\boldsymbol{k}$-space and the effective mass value, which are equivalent to the dependence $E(\boldsymbol{k})$. We will limit the discussion to i) isotropic, spherically-shaped surfaces, ii) single-ellipsoid surfaces, and iii) multi-ellipsoid surfaces. By way of example, we shall consider the conduction band of silicon.

In general, the reciprocal effective mass is a second rank tensor that reduces to a scalar quantity for a spherical band. For a single-ellipsoid model, it is characterized by three values of effective mass, m_i^* (i=1, 2, 3), each corresponding to one of the principal axes of the ellipsoid. In the case of the ellipsoid of revolution, we have only two independent values of the effective mass: $m_{\prime}$* related to the direction of the revolution axis, and $m_{\perp}$* related to the perpendicular axis. In the n-Si-like band model we have 6 equivalent ellipsoids located in $\boldsymbol{k}$-space on the <100>-type axes which are the axes of revolution.

Together with the relaxation time, τ, which is to the first approximation reversal of the collision (scattering) frequency, effective mass determines mobility. The smaller the effective mass, the higher the mobility. For the isotropic band, the carrier mobility is determined by the equation

$$\mu = \frac{e\langle\tau(E)\rangle}{m^*} \tag{5.1}$$

in which $\langle\tau(E)\rangle$ symbolizes averaging τ over the conduction band weighted for a parabolic band by $\mathrm{E}^{3/2}\left(\frac{\partial f_0}{\partial E}\right)$ where f_0(E) is the Fermi-Dirac distribution function. A highly degenerate electron gas, such as a typical TCO, has $(E_F - E_c)/k_BT >> 1$. E_F is Fermi energy, E_c is the energy of the minimum in the conduction band, and k_B is the Boltzmann constant. In such materials $\left(\frac{\partial f_0}{\partial E}\right)$ differs from zero only in the vicinity of Fermi level, hence only the carriers with energies close to Fermi level contribute to electron transport. The properties of these carriers determine the magnitude of the mobility and the other transport coefficients. Thus for an isotropic band, mobility is given by

$$\mu = e\tau(E_F)/m^*(E_F). \tag{5.2}$$

Subsequently, we shall presume high degeneracy, omit the reference to the Fermi level. For an isotropic relaxation time the only reason for the mobility to be anisotropic is anisotropy of the effective mass. For a single ellipsoidal band, the mobility may be expressed as

$$\mu_i = \frac{e\tau}{m_i^*} \tag{5.3}$$

in which the subscript refers to the three principal ellipsoid axes. In polycrystalline material, with randomly oriented crystallites, averaging spatially leads to an isotropic mobility, given by

$$\mu = \frac{1}{3} e\tau \sum_{i=1}^{3} \frac{1}{m_i^*} \tag{5.4}$$

For crystals of cubic symmetry with multi-valley band, such as n-Si or n-Ge, the mobility is isotropic and may be described by

$$\mu = e\tau/m_c^*. \tag{5.5}$$

m_c^* is the *conductivity effective mass* and is determined by

$$\frac{1}{m_c^*} = \frac{1}{3}\left(\frac{1}{m_{\|}^*} + \frac{2}{m_{\perp}^*}\right). \tag{5.6}$$

The factor of 2 inside the parentheses arises because there is rotational symmetry of the ellipsoid in k-space. The conductivity effective mass influences the plasma frequency and, hence, the long-wave limit of transparency of the TCO. The plasma frequency is given by

$$\omega_p = \left(\frac{e^2 N}{m_c^* \varepsilon_\infty \varepsilon_0}\right)^{1/2}, \tag{5.7}$$

where N is the carrier concentration, ε_0 is the free space dielectric constant, and ε_∞ is the high frequency dielectric permittivity of the material.

The density-of-states (DOS) function, $D(E)$ is an important characteristic of a material that also depends on effective mass. For a parabolic band spectrum ($E \alpha k^2$)

$$D(E) = \frac{4\pi(2m_d^*)^{3/2}}{h^3} E^{1/2} \tag{5.8}$$

Here m_d^* is the *density-of-states* (DOS) effective mass, which is a combination of the effective mass components. For the cases of an isotropic spectrum, a single ellipsoid band and a multi-ellipsoidal band, the DOS effective mass is given by equations (5.9) a), b) and c), respectively.

$$m_d^* = m^* \qquad \text{a)}$$

$$m_d^* = (m_1^* m_2^* m_3^*)^{1/3} \qquad \text{b)} \qquad (5.9)$$

$$m_d^* = \mathrm{N}^{2/3}(m_1^* m_2^* m_3^*)^{1/3} \qquad \text{c)}$$

where N is the number of the equivalent ellipsoids, e.g., N=6 for n-Si. It is seen that m_d^* can differ significantly from m_c^*, especially for the multi-ellipsoid model. Comparison of these two values, which may be obtained experimentally, can provide information about the band structure and, in particular, whether it is single- or multi-valley. It can also reveal information about the anisotropy of the constant-energy ellipsoids i.e. about the ratio $\beta = m_{\parallel}/m_{\perp}$.

In turn the DOS function, hence the effective mass, determines the Fermi level for a specific carrier concentration:

$$E_F = \left(\frac{3N}{8\pi}\right)^{2/3}\left(\frac{h^2}{2m_d^*}\right) \qquad (5.10)$$

The change in the position of the Fermi level as a function of carrier concentration, relative to the conduction band minimum, leads to the Burstein-Moss shift [49], which defines the short-wave limit for transparency.

Neglecting the difference between the m_d* and m_c* values can impact estimates of the achievable figure of merit. One must remember that expressions for mobility and plasma frequency include m_c*, while expressions for E_F and hence for the Burstein-Moss shift include m_d*.

5.2.2 Carrier scattering, relaxation time, scattering parameter

Carrier scattering leads to a finite mobility value. The higher the scattering (collision) frequency, hence the lower the relaxation time, the lower the mobility. High scattering rate makes less sharp the plasma reflection edge, thus worsening the transparency spectrum. It also affects absorption by free carriers. Carriers are scattered by phonons, point defects, like vacancies, interstitials, impurity atoms and ions, etc., by dislocations, by two-dimensional defects like small angle boundaries (dislocation walls) or grain boundaries in a very fine granular structures. While the effective mass is considered an intrinsic parameter of a material that depends on its composition, the relaxation time is much influenced by the crystal quality that depends on structural imperfections, hence on the film preparation technique.

Relaxation time depends on the carrier energy (this dependence is different for different scattering mechanisms). In the case of semi-elastic scattering, dependence of scattering frequency on energy can be presented in the form:

$$\tau^{-1}(E) \alpha W(E) D(E) \tag{5.11}$$

where $D(E)$ is the DOS function and $W(E)$ is the square matrix element of the electron scattering giving the probability of transition from one quantum state to another of the same energy. For the most commonly discussed scattering mechanisms, theory shows that, in a parabolic band, $W(E)$ is a power function of energy and is commonly represented as

$$W(E) \alpha E^{-r} \tag{5.12}$$

In a parabolic band, the density of states is given by

$$D(E) \alpha E^{1/2} \tag{5.13}$$

which means that

$$\tau \alpha E^{r-1/2} \tag{5.14}$$

The quantity r is known as the scattering parameter and it is different for each scattering mechanism, varying from r=0 for acoustic phonon scattering, to r=2 for ionized impurity scattering. This kind of dependence, with a fixed value of the scattering parameter, takes place only if the same scattering mechanism dominates over the entire energy range. In reality, several scattering mechanisms may occur simultaneously. The total scattering frequency is the sum of the individual frequencies due to each of the scattering mechanisms, which may be expressed as

$$\omega_c = \tau_c^{-1} = \sum_i \tau_i^{-1} \tag{5.15}$$

The dependence of relaxation time on energy can be more complicated when a wide range of energies is being considered. Fortunately, in the case of high degeneracy (the only practical case for TCOs), only a narrow range of energy around E_F is of interest. In this case *W(E)* can be approximated by a power function

$$W(E) = W(E_F) \times (E / E_F)^{-r} \tag{5.16}$$

The scattering parameter in this case is defined as

$$r(E_F) = \left(\frac{d \ln \tau}{d \ln E} \right)_{E=E_F} + \frac{1}{2} \tag{5.17}$$

Along with the concentration and temperature dependence of mobility, knowledge of the scattering parameter value is important for identifying the dominant scattering mechanism(s).

It is also to be noted that relaxation time depends on the effective mass because of its inverse dependence on the density of states. In heavily doped (degenerate) TCOs, scattering by impurity ions is sometimes the dominant scattering mechanism. In this case, for materials that have the same carrier concentration, density of impurity ions and dielectric permittivity, there can be a difference in mobility because of different effective masses, $\tau \propto 1/m^*$, thus $\mu \propto 1/m^{*2}$.

5.2.3 Influence of non-parabolicity

The dependence $E(k)$ is parabolic only in the immediate vicinity of the conduction band minimum. As energy increases, the dependence deviates from parabolic and the only question is at what energy the deviation becomes sufficiently important to influence the properties of electrons of interest. The most obvious indication of non-parabolicity is the increase of measured effective mass with energy (with Fermi level or carrier concentration in degenerate semiconductors). In narrow-gap, direct-gap semiconductors, such as InSb, (Hg,Cd)Te, PbSe, (Pb,Sn)Te, non-parabolicity significantly affects electronic transport properties at Fermi levels of only $E_F \sim 0.1$eV, or even lower. For wide-gap semiconductors, such as TCOs, non-parabolicity has not been much investigated but for heavily doped ZnO, CdO, and zinc stannate it has been established that there is a progressive increase of the density-of-states effective mass with carrier concentration [46-48].

To analyze the influence of non-parabolicity, we consider the theory of electron transport developed in [50, 51] for the rather general, multi-ellipsoid, non-parabolic band model. The equations for the transport coefficients are based on solutions of the Boltzmann equation and the relaxation time approximation.

In [50, 51] the energy dependence on wave vector in the principal ellipsoid axes (1, 2, 3) is described by the equation:

$$\frac{\hbar^2}{2}\left[\frac{k_1^2}{m_{10}^*}+\frac{k_2^2}{m_{20}^*}+\frac{k_3^2}{m_{30}^*}\right]=\gamma(E)=E\left(1+\frac{E}{E_1}+\frac{E^2}{E_2^2}+\frac{E^3}{E_3^3}+\cdots\cdots\right) \qquad (5.18)$$

where m_{i0}^* (i=1, 2, 3) are the effective mass components at the bottom of the band (E=0). $\gamma(E)$ is an arbitrary function of energy which may be represented as a power series in energy with coefficients given by E_1, E_2^2, E_3^3, etc. The latter have dimensions of energy raised to the same power as their energy term in each numerator. The values of E_1, E_2, E_3, etc., determine the deviation of the spectrum from parabolic for each energy E. If $E \ll E_1, E_2, E_3$, etc., the equation reduces to that of a parabolic band. We will refer to first order non-parabolicity as the case when

$$\gamma(E) \approx E\left(1+\frac{E}{E_1}\right) \qquad (5.19)$$

in the energy range of interest, while the terms of higher in energy power can be neglected.

For the non-parabolic spectrum, the equations for the effective masses, density of states function and carrier concentration are

$$m_i^*(E) = m_{i0}^* \frac{d\gamma}{dE} \qquad \text{a)}$$

$$m_c^*(E) = m_{c0}^* \frac{d\gamma}{dE} \qquad \text{b)} \qquad (5.20)$$

$$m_d^*(E) = m_{d0}^* \frac{d\gamma}{dE} \qquad c)$$

$$D(E) = \frac{4\pi\left(2m_{d0}^*\right)^{3/2}}{h^3}\left[\gamma(E_F)\right]^{1/2}\frac{d\gamma}{dE} \qquad (5.21)$$

$$N = \frac{8\pi}{3}\frac{\left(2m_{d0}^*\right)^{3/2}}{h^3}\left[\gamma(E_F)\right]^{3/2} \quad \text{(high degeneracy)} \qquad (5.22)$$

It is seen that the effective mass increases with energy since $d\gamma/dE > 0$. The density of states grows more rapidly with energy and Fermi level increases slower with the carrier concentration than in a parabolic band.

Non-parabolicity changes the relaxation time dependence on energy. One of the reasons is the change in the $D(E)$ dependence. The scattering matrix element is preserved in [51] with the same dependence as in the parabolic case, $W(E) \propto \left(k^2\right)^{-r}$, with the same values of the scattering parameter r for each particular scattering mechanism. Thus, based on equation (5.21), one obtains for the non-parabolic spectrum

$$\tau \propto \left[W(E)D(E)\right]^{-1} \propto \gamma^{r-1/2}\left(\frac{d\gamma}{dE}\right)^{-1} \qquad (5.23)$$

instead of $\tau \propto E^{r-1/2}$ for the parabolic band.

The above analysis shows that we need to know the real dependence, ***E(k)***, when trying to estimate the limiting value of mobility, μ_{lim}, for heavily doped TCOs. Using, for example, the effective mass obtained from a sample of a not-too-high carrier concentration, one can overestimate μ_{lim} for a material with a more practical carrier concentration. The same is true for the plasma frequency and the Burstein-Moss shift. Analysis of the transport phenomena, aimed at establishing the dominant scattering mechanism, can lead to the wrong conclusions if parabolic theory is applied to a material while the spectrum is actually non-parabolic.

5.3 Method of Four Coefficients (Electron Transport in Stationary External Fields).

As mentioned in Sec.5.1 the method discussed in this section is aimed at the determination of mobility, the DOS effective mass, m_d^*, and the scattering parameter, r. It is based on the simultaneous measurements of four transport coefficients: electrical resistivity, ρ, the Hall,

Seebeck, and Nernst-Ettingshausen coefficients, R_H, α, and Q, respectively (ρ and α at $\boldsymbol{B}$=0 and R_H and Q in a weak magnetic field).

Hall effect measurements provide the carrier concentration. In a weak magnetic field ($\mu B << 1$),

$$R_H = A_R / qN , \tag{5.24}$$

where $q = -e$ for electrons and $q = e$ for holes. The Hall factor, A_R, which is isotropic for spherical and single-ellipsoid constant-energy surfaces, is very close to 1 in the case of high degeneracy. For a multi-ellipsoid band in cubic crystals (like n-Si and n-Ge) it is also isotropic but its value depends on the anisotropy of the ellipsoids. It is given by

$$A_R = \frac{3\beta(\beta+2)}{(2\beta+1)^2}, \tag{5.25}$$

where

$$\beta = \frac{m_{\parallel}}{m_{\perp}} \tag{5.26}$$

This brings some uncertainty in the determination of N, but fortunately not too high. For example, A_R=0.96 for β=2, and A_R=0.82 for β=10.

Combined measurements of ρ and R_{H} provide an estimate of the mobility. The so-called Hall mobility differs from the real drift mobility by the Hall factor, A_R. Hence,

$$\mu_H = |R| / \rho = A_R \mu \tag{5.27}$$

Combined measurement of Hall coefficient (carrier concentration) and Seebeck coefficient (thermopower) is one of the oldest methods used to estimate the effective mass in semiconductors. For a parabolic band and high degeneracy, the Seebeck coefficient is given by

$$\alpha = 8\pi\left(\frac{\pi}{3}\right)^{5/3} \frac{k_B^2 T}{qh^2}(r+1)\frac{m_d^*}{N^{2/3}} \tag{5.28}$$

Equation (5.28) contains one more quantity to be determined, namely the scattering parameter, r. Using this equation without knowledge of the value of the scattering parameter, can lead to a rather inaccurate estimate of m_d^*. For example, if one assumes that the dominant scattering mechanism is due to acoustic phonons, for which r=0, one will obtain a value of m_d^* three times greater than that obtained if one assumes ionized impurity scattering, for which r=2.

The problem can be solved by measuring the resistivity and the transverse Nernst-Ettingshausen (N-E) coefficient along with the Hall and Seebeck coefficients. The thermo-magnetic N-E effect is defined by the equation [52]:

$$E_y = -Q\frac{dT}{dx}B_z . \tag{5.29}$$

For a parabolic band and with high degeneracy of the carrier gas, the N-E coefficient can be described by

$$Q = |\alpha|\mu_H \frac{r-1/2}{r+1} \tag{5.30}$$

Combining Eqs. (5.28) and (5.30), one obtains

$$m_d^*(E_F) = \left(\frac{3N}{8\pi^4}\right)^{2/3} \frac{eh^2}{k_B^2 T}\left(|\alpha| - \frac{Q}{\mu_H}\right) \tag{5.31}$$

and

$$r = \frac{3}{2}\frac{Q}{|\alpha|\mu_H - Q} + \frac{1}{2} \tag{5.32}$$

Thus, by measuring the four transport coefficients, one can determine both the DOS effective mass and scattering parameter. In the non-parabolic case equations (5.28) and (5.30) transform to

$$\alpha = 8\pi\left(\frac{\pi}{3}\right)^{5/3} \frac{k_B^2 T}{qh^2}\frac{1}{N^{2/3}}\left[m_d^*(r+1-\lambda)\right]_{E_F} \tag{5.33}$$

and

$$Q = |\alpha|\mu_H\left(\frac{r-1/2-\lambda}{r+1-\lambda}\right)_{E_F} \tag{5.34}$$

where

$$\lambda(E) \equiv 2\gamma(E)\frac{d^2\gamma}{dE^2}\left(\frac{d\gamma}{dE}\right)^{-2} = \frac{N}{m_d^*}\frac{dm_d^*}{dN} \tag{5.35}$$

It is easy to show that m_d^* can be calculated from the measured data using the same equation (5.31) as in the parabolic case. The scattering parameter is now defined as

$$r = \frac{3}{2}\left(\frac{Q}{|\alpha|\mu_H - Q}\right) + \frac{1}{2} + \lambda \tag{5.36}$$

To realize all the advantages offered by this method, we must have heavily doped samples of a material in a wide range of carrier concentrations/Fermi level positions. Based on measurements of the four transport coefficients, we are able to obtain the dependence $m_d^* = f(N)$.

If $m_d^*(N) = const$, the deviations from parabolicity are negligible in this range of N and E_F, and, in subsequent analysis, we may reasonably use parabolic band theory. A substantial increase in m_d^* with carrier concentration indicates the need to use the more general non-parabolic band theory. Using the experimental dependence $m_d^* = f(N)$, with equations (5.20) – (5.22), we can reconstruct the function $\gamma(E)$ and, hence, $E(k)$. The scattering parameter data enable us to identify the dominant scattering mechanism and to monitor its changes as a function of carrier concentration.

It should be mentioned here that the empirically established correlation, $\alpha \sim N$, can be used to map the carrier concentration distribution over the sample area of a thin film. Measurement of the local Seebeck coefficient, at various positions on the surface, by relocating the thermoprobe, is a non-destructive and simple method that may be applied to films of an arbitrary size and shape.

5.4 Combining the Four-Coefficient Method with Optical Characterization (Ultra-High Frequency Electron Transport).

5.4.1 Basics of optical method. Conductivity effective mass. Optical mobility

The high electrical conductivity in metals and heavily doped semiconductors, and its dependence on frequency, significantly influences the optical properties of these materials and, in particular, the transmittance and reflectance spectra. The electrical conductivity is a complex value and depends on frequency of the electric field. It is given by

$$\sigma(\omega) = \frac{\sigma_0}{1 - i\omega\tau} \tag{5.37}$$

where σ_0 is the stationary (DC) conductivity, which is defined as

$$\sigma_0 = e^2 N \tau / m_c^* \tag{5.38}$$

The real and imaginary parts of the dielectric permittivity are described by equations:

$$\mathrm{Re}\,\varepsilon = \varepsilon' = n^2 - k^2 = \varepsilon_\infty \left(1 - \frac{\omega_p^2}{\omega^2 - \omega_c^2}\right), \tag{5.39}$$

and

$$\mathrm{Im}\,\varepsilon = \varepsilon'' = 2nk = \varepsilon_\infty \left(\frac{\omega_p^2 \omega_c}{\omega\left(\omega^2 + \omega_c^2\right)}\right). \tag{5.40}$$

n and k are the refractive index and extinction coefficient, respectively, ε_∞ is the "high-frequency" dielectric permittivity due to the bound electrons. Two characteristic frequencies: ω_p and ω_c, are totally defined by the free carriers. The plasma frequency, ω_p, is related to the carrier concentration and conductivity effective mass by equation (5.7). The collision frequency, ω_c, is the reciprocal of the relaxation time, $\omega_c = 1/\tau$.

When the frequency of an electromagnetic wave, ω, decreases so that it is close to ω_p, reflectance and transmittance of the material change dramatically. If $\omega_c << \omega_p$, then, to a first approximation,

$$\varepsilon \approx \varepsilon' = \varepsilon_\infty \left(1 - \omega_p^2 / \omega^2\right) \tag{5.41}$$

When ε is real and negative ($\omega < \omega_p$), the solutions to the wave equation decay exponentially in the material; i.e. no radiation can propagate. Thus at $\omega = \omega_p$, a sharp increase in reflectivity, known as the "plasma reflectivity edge", should be observed. For real conductors, ω_c/ω_p is usually not so small, therefore reflectance does not change so rapidly when the frequency approaches ω_p. The analysis of the measured optical spectra (by, for example, spectrophotometry or ellipsometry) allows the plasma and collision frequencies to be determined.

Based on the plasma frequency and Hall carrier concentration data, it is possible to calculate the conductivity effective mass, m_c^*, using equation (5.7). Comparison of m_c^* with m_d^* (see Section 5.2.1) provides guidance about the shape of the constant-energy surfaces, and, in particular, enables a distinguishing between the single-valley and multi-valley models. For a single-ellipsoid model this comparison enables an approximate estimation of the deviation from the spherical shape. In principle, measuring dependence $m_c^*(N)$ provides establishing of non-parabolicity and reconstruction of $\gamma(E)$ and $E(k)$ dependencies in the same way as $m_d^*(N)$. Coincidence of the obtained results could be considered as an evidence of their reliability, which is important because each of the methods used separately has in general its own sources of errors both technical (like non-accurate measurements, not-to-high uniformity of the samples) and theoretical (validity of the theories behind the methods).

The empirically established dependence, $\omega_p(N)$ for a particular material provides an alternative to the Hall effect method for measuring carrier concentration and its uniformity over the thin film area. Multi-angle spectral ellipsometry, with appropriate modeling of the raw data, provides a unique option to test the uniformity of N and μ (via ω_p and ω_c) over the film thickness [53].

Based on the m_c^* and ω_c data, derived from the optical characterization, one can calculate the *optical mobility* defined as

$$\mu_0 = \frac{e\tau}{m_c^*} = \frac{e}{m_c^* \omega_c}, \tag{5.42}$$

which is not necessarily the same as the Hall mobility. Comparison of the two provides guidance about contribution of the grain boundaries to the measured DC sheet resistance and bulk resistivity.

5.4.2 Evaluation of the grain boundary contribution to the film sheet resistance.

A significant difference is usually observed between resistivity measured on a single crystal and thin film polycrystalline samples of the same semiconductor with the same carrier concentration. This difference is commonly attributed to the influence of grain boundaries (GB). It is accustomed to treat the problem in terms of the "GB scattering". This terminology is not always correct and sometimes can be misleading. Indeed, GB disturb the translation symmetry of the crystal and inevitably cause the free carrier scattering. But the GB scattering coexists with scattering by phonons, point defects, dislocations, etc. The total scattering rate is the sum of the particular ones. The contribution of GB scattering is significant only if the grain size, d, is comparable to the mean free path, l, due to all the scattering mechanisms. In typical polycrystalline thin TCO films the l value estimated based on the mobility and carrier concentration is rather small: $l \delta 100$Å, while $d \tau$ 1000Å.

Thus, we have to use a different approach to the problem. We must regard a TCO polycrystalline film as having two phases. One of these is the material inside the grains (bulk material), and the other is that at grain boundaries. The equivalent electrical circuit of the sample can be constructed as a series connection of resistors, R_B and R_{GB}, representing bulk material and grain boundaries, respectively. When measuring the DC resistance of the film, we obtain the sum of these two types of resistors. Thus the measured bulk resistivity, ρ, relates to the real resistivity in the grain bulk, ρ_B, as

$$\rho = \rho_B \left(1 + R_{GB} / R_B\right). \tag{5.43}$$

The R_{GB}/R_{GB} ratio can be estimated based on comparison of the optical and Hall mobilities. Scattering in the grain bulk dominates the collision frequency, ω_c, if the grain size, d, is much greater than the mean free path, l, which is the case for TCOs. Thus the optical mobility defined by Eq. (5.42) is close to the real drift mobility in the grain bulk. The Hall mobility is determined by the Hall coefficient and DC resistivity measurements: $\mu_H = R_H / \rho$. Hence the measured Hall mobility due to the influence of GB can differ significantly from the real mobility in the grain bulk. Supposing the Hall factor $A_H \approx 1$ and using Eqs. (5.42) and (5.43), we obtain the equation that enables estimation of the GB contribution to the resistivity:

$$\frac{R_{GB}}{R_B} = \frac{\mu_o}{\mu_H} - 1 \tag{5.44}$$

This method has been applied to the evaluation of the grain boundary contribution in several TCOs. It was found that for the relatively high carrier concentration materials, ($N \tau$ 3x10^{20}cm^{-3}), $\mu_o \approx \mu_H$, that is $R_{GB}/R_B << 1$. On the other hand, films with much lower carrier concentrations, demonstrated a considerable difference between μ_o and μ_H, thereby indicating the impact of grain boundaries.

These results are consistent with a model widely used to explain the enhanced resistance of grain boundaries. The electrical charge located at grain boundaries, due to trapping of majority carriers

by the electron states, creates a potential barrier for free carriers and increases the resistance of the grain boundary regions. With increasing doping level, the amount of the trapped charge also increases, as does the height of the potential barrier. With the further increase in doping level, eventually all the grain boundary states are filled with trapped carriers and the charge cannot increase any more. However the space charge density in the depletion region continues to increase causing a reduction in the height and width of the potential barrier, making it transparent to carrier tunneling. Moreover, for a very high doping level, the potential barrier is well below the Fermi level and the electrons pass over the barrier without being remarkably perturbed by it [55, 56].

It should be mentioned here that the other method for studying electrical properties of the GB described in Sec. 4, namely Impedance Spectroscopy, is not applicable to the high conductivity TCO films. The limitation is put by the value of the product of the film resistance and capacitance which defines characteristic frequency of the sample, $\omega_o=(R_{sh}C_{sh})^{-1}$. Here R_{sh} ($\Omega/\square$) and C_{sh}($F/\square$) are the sheet resistance and sheet capacitance of the film. For the 1 μm thick film with a grain size of 1 μm, $R_{sh} \sim 10\ \Omega/\square$ and $C_{sh} \sim 0.1$ pF/□. Thus, $\omega_o \sim 10^{12}$ rad/s = 160 GHz which is far beyond the frequency limit of our LCR meters.

5.5 Four Coefficient Measurements.

5.5.1 Measurement techniques and experimental procedure

The four-coefficient instrument created at NREL has already been described and discussed in detail in [45, 47]. Here we present only a brief review of its principal features and operation.

Thin film TCO samples are deposited on electrically insulating substrates and are etched photolithographically to the pattern schematically shown in Fig. 5.1b. Two copper blocks with embedded electrical heaters control the sample temperature and the temperature gradient in vertical direction when measuring Seebeck and Nernst-Ettingshausen (N-E) effects. The copper blocks have a differential thermocouple mounted between them to measure the temperature gradient across the sample. One of the blocks has an additional embedded thermocouple for absolute temperature measurement. The entire sample holder is cooled by a closed-cycle helium cryostat for temperature-dependent measurements from 30 to 350 K.

Hall effect and resistivity are measured with the van der Pauw method by using electrical contacts 1, 2, 3, and 4. The Seebeck voltage is measured between contacts 1 and 3, and N-E voltage is measured between contacts 2 and 4. Note that the temperature gradient is applied parallel to the short dimension of a sample while the N-E voltage is measured in the long dimension. This geometry of the sample orientation is different from the traditional geometry (see, e.g., [52]) presented schematically at Fig. 5.1a. The latter is similar to the Hall bar geometry where current flows along the long side of a sample and Hall voltage is measured along the short side. The reason for changing geometry is that the N-E coefficient is very small in TCOs. Indeed, this coefficient is proportional to mobility and the ratio $k_BT/(E_F-E_C)$, see Sec.5.3. Both parameters are small for typical TCOs, so that for the reasonable values of magnetic field and temperature difference across the sample, the N-E signal is in the nano-volt scale.

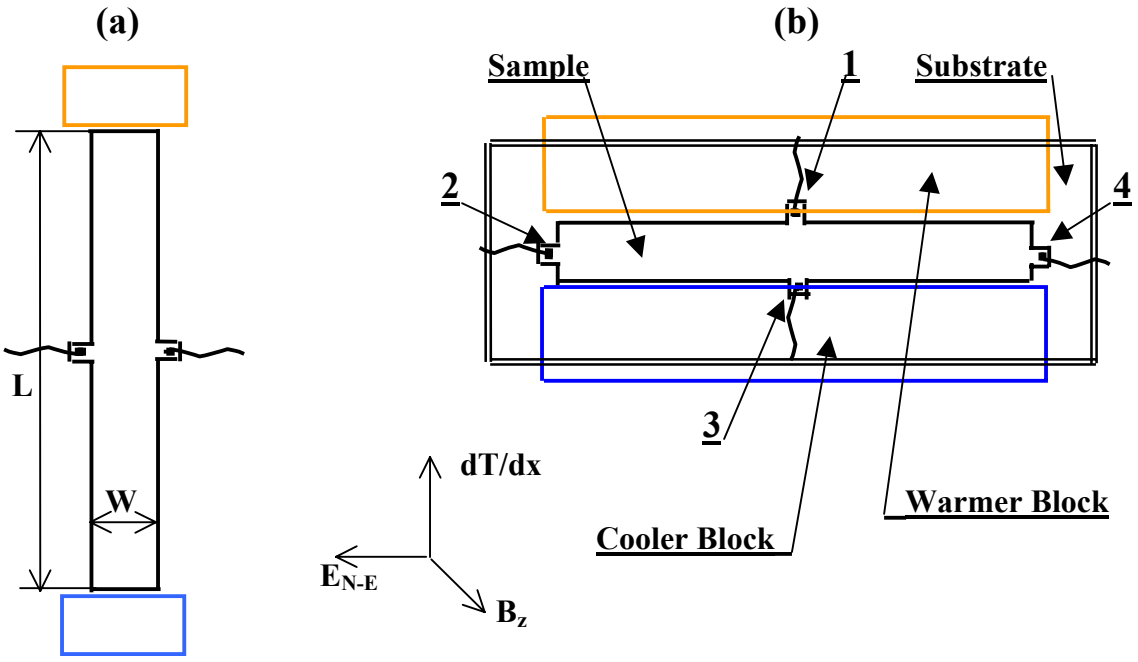

Fig. 5.1 Comparison of two types of geometry used for the N-E effect measurements. (a) traditional geometry; (b) geometry used in our instrument.

Let us rewrite the equation (5.29) for the N-E effect in terms of temperature difference across a sample, $\Delta T=(dT/dx)L$, and the N-E voltage, $V_{N-E}=E_{N-E}W$, where L and W are the sample dimensions shown in Fig. 5.1a. The new equation is

$$V_{N-E} = Q \times \Delta T \times B_z \times \frac{W}{L} \qquad (5.45a)$$

For the geometry shown in Fig. 5.1b this equation transforms to

$$V_{N-E} = Q \times \Delta T \times B_z \times \frac{L}{W} \qquad (5.45b)$$

where L and W are the lengths of the long and short sides of a sample respectively. It is see that rotation of the sample by the angle of 90^o with respect to the temperature gradient direction leads to the $(L/W)^2$ fold increase in the N-E signal. For the real samples we use, L=16 mm and W=3mm, that is $(L/W)^2=28.4$. Thus using the geometry of Fig. 5.1b we provided a significant increase in the N-E voltage while preserving a reasonably small temperature difference across the sample, of 10 K or less. This geometry was proposed and realized first in [57].

5.5.2 Some results and discussion

To demonstrate applicability of the method to studies of TCOs and illustrate typical information provided by these measurements, we review here briefly the data obtained for ZnO thin films and presented in [47].

The films were RF magnetron-sputtered on 7059 glass substrates. The DOS effective mass m_d* was studied with the FC method in the carrier concentration range of $2x10^{19}$ to $5x10^{20}$ cm^{-3}. The obtained value of m_d* varies in this range from 0.3 to 0.45 m_e indicating non-parabolicity of the conductance band. The plot of m_d* vs. $N^{2/3}$ is linear indicating the first-order non-parabolicity in this concentration range. Extrapolation of the plot to N =0, provided m_{do}*=0.27m_e (m_{do}* is the DOS effective mass at the conduction band bottom). The plasma-frequency conductivity effective mass values for the electron concentrations of $4x10^{19}$ and $5x10^{20}$ cm^{-3} taken from literature [58, 59] are in a good agreement with m_d*. Namely, it regards the deviation from the parabolic spectrum. Besides, the difference between m_d* and m_c* is rather small which corresponds to the single-valley band in agreement with the theory prediction [60]. The constant-energy shape is close to sphere. Within the accuracy of measurements the ratio of the ellipsoid principal axes lengths does not exceed 1.5.

The scattering parameter r values were determined as described in Sec. 5.3, using Eq. (5.36) with the non-parabolicity parameter λ (Eq. (5.35) values derived from the experimental dependence $m_d^*(N)$. For heavily doped ZnO:Al samples ($N \geq 4x10^{20}$ cm^{-3}) the r value matches well with that for the impurity ion scattering. For the undoped material ($N \sim 2x10^{19}$ cm^{-3}), the scattering parameter was found to lie closely with the neutral impurity trend.

It is interesting to compare data for ZnO with those for Cd_2SnO_4 (CTO). CTO films were also prepared with the RF magnetron sputtering. Free electron concentration varied between $2x10^{20}$ and $6.8x10^{20}$ cm^{-3}. The DOS effective mass increases with the carrier concentration, but much slower than in ZnO, only by a factor of 1.2 in the concentration range indicated above. The m_d* value in CTO is smaller than in ZnO, by a factor of 1.8 for N =$4x10^{20}$ cm^{-3}. Probably this difference accounts for mobilities in CTO being nearly 3 times larger than in ZnO. First, mobility is reversely proportional to effective mass, and second, the lower effective mass, and hence lower density of states leads to the reduced scattering rate. Indeed, the estimated relaxation time value for N= $4x10^{20}$ cm^{-3} in CTO is ~1.6 times that value for ZnO. It is important to point that comparison of the Hall and optical mobilities in both materials differ only slightly indicating no considerable impact of grain boundaries on the film sheet resistance. The same conclusion was made previously in [53, 54] about SnO_2:F films.

5.6 Conclusions

Based on the data above, as well as on the other presented in [44-48], one can conclude that the FC method is a good experimental technique for studies of TCO films, especially if combined with the plasma and collision frequencies measurement. This method can be applied to other materials, heavily or slightly doped, both in bulk and thin film form. The equipment built at NREL for measuring the four transport coefficients, demonstrated its high quality and capability to characterize materials difficult to measure due to low mobility and high degeneracy, such as TCOs. So much the better it could be used for characterization of materials with more favorable properties.

6. References

1. K. D. Dobson, I. V. Fisher, G. Hodes and D. Cahen, *Solar Energy Mater. & Sol. Cells* **62**, 295-325 (2000).

2 J. Tang, D. Mao, T. R. Ohno, V. Kaydanov and J. U. Trefny, *Proc. 26th IEEE PVSC*, Sept.–Oct. 1997, Anaheim, CA, pp 439-442.

3. W. Song, D. Mao, Y. Zhu, J. Tang and J. U. Trefny, *Proc. 25th IEEE PVSCP*, May 1996, Washington, DC, pp 873-876

4. H.C. Chou, A. Rohatgi, E.W. Thomas, S. Kamra, A.K. Bhat, *J. Electrochem. Soc*. **142**, 254 (1995)
5. S.E. Asher, R.C. Reedy, Jr., R. Dhere, T.A. Gessert, M.R. Young, *NCPV Progr. Rev. Meeting 2000*, April 2000, Denver, CO, p.275

6. T.P. Thorpe, Jr., A.L. Fahrenbruch, and R.H. Bube, *J. Appl. Phys*. **60**, 3622 (1986)

7. L.M. Woods, D.H. Levi, V. Kaydanov, G.Y. Robinson, R.K. Ahrenkiel*, Proc. 2nd World Conf. on PV Solar Energy Conversion*, July 1998, Vienna, Austria, p.1043.

8. A.S. Gilmore, V. Kaydanov, U. Laor, A. Gupta, T.R. Ohno, B. McCandless, *NCPV Progr. Rev. Meeting 2000*, April 2000, Denver, CO, p.259.

9. E.Kucys, J. Jernot, K. Bertulis, and V. Bariss, *Phys. Stat. Sol*.**A 59**, 91 (1980).

10. G. Zoth, F.G. Reidel, W. Schroter, *Phys. Stat. Sol*. **B 172**, 187 (1992).

11. F. Abou-Elfotouh, S. Ashour, S.A. Alkuhaimi, J. Zhang, D.J. Dunlavy, L.L. Kazmersky, *Mat. Res. Soc. Symp. Proc*. **238**, 335, (1992).

12. A. Castaldini, A. Cavalinu, B. Fraboni, P. Fernandez, J. Piqueras, *J. Appl. Phys*. **83**, 2121 (1998).

13. D. Mao, L. H. Feng, Y. Zhu, J. Tang, W. Song, R. Collins, D. L. Williamson, and J. U. Trefny, *13th NREL PV Program Review Proc*., AIP Conference Proc. 353, p.352 (1996).

14. M. H. Aslan, W. Song, J. Tang, D. Mao, R. T. Collins, D. H. Levi, R. K. Ahrenkiel, S. C. Lindstrom, and M. B. Johnson, *Mat. Res. Soc. Symp. Proc*., **485** p.203 (1998).

15. H.C. Chou, A. Rohatgi, N.M. Jokerst, E.W. Thomas, S. Kamra, *J. Electron. Mater*. **25,** 1093 (1996).

16. P. Blood and J.W Orton, "The Electrical Characterization of Semiconductors: Majority Carriers and Electron States", Academic Press, 1992.

17. Ahmet Balcioglu, "Characterization of Deep Impurity Levels in Semiconductor Devices", Ph.D. Thesis, Department of Physics, Colorado School of Mines, Golden, CO, 2000.

18. A. Balcioglu, R.K. Ahrenkiel and F. Hasoon (submitted for publication to *J.Appl. Phys*., 2000).

19. S.S. Ou, A. Bindal, O.M. Stafsudd, and K.L. Wang, *J. Appl. Phys*. **55**, 1020 (1984).

20. M.A. Lourenco, Y.K. Yew, K.P. Homewood, K. Durose, H. Richter, and D. Bonnet, *J. Appl. Phys*. **82**, 1423 (1997).

21. M.A. Lourenco, W.L. Ng, K.P. Homewood, and K. Durose, *Appl. Phys. Lett*. **75**, 277 (1999).

22. K. Zanio, "Semiconductors and Semimetals", Volume 13, Academic Press, 1978.

23. A.J. De Nobel, *Phil. Re. Rep*. **14**, 430 (1959).

24. D.G. Jensen, B.E. McCandless and R.W. Birkmire, *Proc. 25th IEEE PVSC*, Washington, DC, May 1996, p. 773.

25. G.A. Valaskovic, M. Holton and G.H. Morrison, *Applied Optics* **34**, 1215 (1995).

26. E. Betzig, P.L. Finn and J.S. Weiner*, Appl. Phys. Lett*. **60**, 2484 (1992).

27. K. Ohata, J. Saraie and T. Tanaka, *Jap. J. Appl. Phys*. **12**, 1641 (1973).

28. D.S. Albin, private communication.

29. O. deMelo, M.Melendez-Lira, I. Hernandez-Calderon, L. Banos, and A. Morales-Acevedo, Proc. *1st IEEE World Conf. on Photovoltaic Solar Energy Conversion*, New York,1994, p.369.

30. M.S. Unlu, B.B. Goldberg, W.D. Herzog, D. Sun and E. Towe, *Appl. Phys. Lett*. **67**, 1862 (1995).

31. J.J.. Kester, S. Albright, V. Kaydanov, R. Ribelin, L.M. Woods, J.A. Philips*, NREL/SNL PV Program Review, Proc 14th Conf*., Lakewood, CO, 1996, p. 162.

32. V.I Kaydanov and T.R Ohno, "Process Development and Basic Studies of Electrochemically Deposited CdTe-Based Solar Cells", Colorado School of Mines, Annual Technical Report to NREL, Subcontract No. XAK-8-17619-28, Phase I, 15 May 1998-14 May 1999.

33.Y. Matukura, *Jpn. J. Appl. Phys*. **2**, 91 (1963).

34. W.E. Taylor, N.H. Odell, and H.Y. Fan, *Phys. Rev*. **88**, 867 (1952);
R. Stratton, *Proc. Phys. Soc*., London, **B 69**, 513 (1956).

35. M.G. Spencer, W.J. Schaff and D.K. Wagner, *J. Appl. Phys*. **54**, 1429 (1983)

36. M. Matsuoka, *Jpn. J. Appl. Phys*. **10**, 736, (1971);
L.M. Levinson and H.R. Philipp, *J. Appl. Phys*. **46**, 1332(1975).

37. G.E. Pike and C.H Seager, *J.Appl. Phys*. **50**, 3414 (1979).

38. C.H. Seager and G.E. Pike, *Appl. Phys. Lett*. **37**, 747 (1980).

39. G.E. Pike, "Grain Boundaries in Semiconductors", Elsevier Science Publ. Co., Inc., 1982, p. 369.

40. M.K. Zhitinskaya, V.I. Kaidanov, and I.A. Chernik, *Sov. Phys. Solid State* **8**, 295 (1966).

41. I.A. Chernik, V.I. Kaidanov, E.P. Ishutinov, *Sov. Phys. Semicond.* **2**, 825, (1969).

42. I.A. Chernik, V.I. Kaidanov, M.I. Vinogradova, and N.V. Kolomoets, *Soviet Physics-Semiconductors* **2**, No.6, pp. 645-651 (1969).

43. T.S. Gudkin, V.I. Kaidanov, et.al., *Sov. Phys. Semicond.* **5**, 1089 (1971).

44. W.P. Mulligan, "A Study of the Fundamental Limits to Electron Mobility in Cadmium Stannate Thin Films", Ph. D. Thesis, Department of Physics, Colorado School of Mines, Golden, CO, 1997.

45. D.L. Young, T.J. Coutts, V.I. Kaydanov, *Rev. of Sci. Instr*. **71**, 462 (2000).

46. T.J. Coutts, D.L. Young and X. Li, *MRS Bulletin*, **25**, No.8, 58 (Aug. 2000).

47. D.L. Young, T.J. Coutts, V.I. Kaydanov, W.P. Mulligan, to be published in *J. Vac. Sci. Technol.* **A 18,** No. 6, Nov-Dec. 2000.

48. D.L. Young, "A Fundamental Study of Electron Transport in Zinc Stannate Thin Films", Ph.D Thesis, Department of Physics, Colorado School of Mines, Golden, CO, 2000.

49. E. Burstein, *Phys. Rev.* **93**, 632 (1954).

50. J. Kolodziejchak and S. Zhukotynski, *Phys. Status Solidi* **5**, 145 (1964).

51. W. Zawadski and J. Kolodziejchak , *Phys. Status Solidi* **6**, 419 (1964).

52. E. Putley, "The Hall Effect and Related Phenomena", Butterworths, London, 1960.

53. A. M. Alkaoud, "APCVD Preparation and Studies of Physical Properties of Tin Oxide Thin Films", Ph. D. thesis, Department of Physics, Colorado School of Mines, Golden, CO, 1999.

54. A. Al-Kaoud, T. Wen, A. Gilmore, V. Kaydanov, T.R Ohno, C. Wolden, L. Feng, J. Xi, *NCPV Progr. Rev., Proc. 15th Conf.*, Denver, CO, 1998, p.212.

55. T.S Gudkin, I.A. Drabkin, V.I. Kaidanov, O.G. Sterlyadkina, *Sov. Phys. Semicond.* **8**, 1453 (1975).

56. L.I. Bytenskii, S.A. Kaz'min, V.I. Kaidanov, Yu.I. Ravich, and A.V. Savel'ev, *Sov. Phys. Semicond.* **16**, 712 (1982).

57. V.I. Kaidanov and I.A. Chernik, *Sov. Phys. Semicond.* **1**, 1159 (1967).

58. S. Brehme, F. Fenske, W. Fuhs, E. Nebauer, M Poschenrieder, B. Selle, and I. Sieber, *Thin Solid Films* **342**, 167 (1999).

59. K.H. Hellwege, "Landolt-Bornstein numerical data and functional relationships in science and technology: Semiconductors", in *Numerical Data and Functional Relationships in Science and Technology*, edited by O. Madelung, M. Scultz, and H. Weiss (Springer, Berlin, 1982), vol. 17.

60. S. Bloom and I. Ortenburger, *Phys. Status Solidi* **B 58**, 561 (1973).

7. Acknowledgements

Many people, in addition to those at the Colorado School of Mines, have contributed to this work over the past year. We are thankful to Rick Powell, Doug Rose, Victor Karpov, Don Grecu, and Upali Jayamaha of First Solar, LCC., for supplying us with the materials for CdTe/CdS cells preparation and for thin film studies. It is hard to underestimate the value of discussions of our research approach and results that we have had with the individuals mentioned above and also Bolko von Roedern, Tim Gessert, Dave Albin, Peter Meyers, and other scientists involved in fabrication and studies of thin film solar cells. We greatly appreciate the encouraging interest in our activities, discussions and suggestions we get constantly from Kenneth Zweibel, Harin Ullal, and especially from our contract monitor, Bolko von Roedern.

8. Appendices

8.1 Personnel

The names, titles, and representative responsibilities of the individuals contributed to this work are summarized below.

Timothy R. Ohno, Associate Professor of Physics: Photovoltaic Development, Surface Physics, Principal Investigator

Victor I. Kaydanov, Research Professor of Physics: Photovoltaic Development, Electron Transport Phenomena, Principal Investigator

Reuben T. Collins, Professor of Physics: Electronic and Optical Properties of Semiconductors

Don L. Williamson, Professor of Physics: Structural Properties of Materials, XRD

Thomas E. Furtak, Professor of Physics: Optical Properties of Semiconductors, Ellipsometry

Dr. Timothy J. Coutts (NREL): Electronic and Optical Properties of Semiconductor Materials and devices

Dr. Richard K. Ahrenkiel (NREL), Adjunct Professor of Physics: Electronic and Optical Properties of Semiconductor Materials and Devices

Dr. Dean H. Levi (NREL): Electronic and Optical Properties of Semiconductor Materials and Devices

Dr. Akhlesh Gupta, Post. Doc.: CdTe Cell Processing and Characterization

Angelo S. Gilmore, Graduate Research Assistant: Impedance Spectroscopy, Hall effect

Scott Townsend, Graduate Research Assistant: ZnTe Back Contact, Cell Stability

Mary K. Herndon, Graduate Research Assistant: Near Field Scanning Optical Microscopy (defended Ph.D. thesis November 1999)

Ahmed Balcioglu, Graduate Student: Deep Level Transient Spectroscopy (defended Ph.D. thesis August 2000)

David L. Young, Graduate Student: Electron Transport Phenomena in Semiconductors
(defended Ph. D. thesis August 2000)

Brian Egaas, Graduate Research Assistant: Thin Film Solar Cell Fabrication

Wendi Batchelor, Graduate Research Assistant: Thin Film Solar Cell Fabrication

Don Robb Sparks, undergraduate student, degradation chamber design

8.2 Laboratory Improvements

Some laboratory improvements occurred during Phase II of this subcontract that have permitted more thorough materials characterization.

A Hewlett-Packard LCR meter, Model 4284A (20 Hz - 1 MHz) was added to the H-P LCR meter, Model 4285A (75 kHz-30 MHz) we possessed previously. Broadening of the frequency range provides more opportunities for studying electronic properties thin films and solar cells using the impedance spectroscopy method.

Building of the near field scanning optical microscope was completed, which enabled studying and mapping optical and electronic properties of the cell with the spatial resolution of ~100 nm.

8.3 Publications/Presentations

1. D.L. Young, T.J. Coutts, V. I. Kaydanov, "Density-of-states effective mass and scattering parameter measurements by transport phenomena in thin films", *Rev. of Sci. Instr.* **71**, pp. 462-466 (2000).

2 A.S. Gilmore, V. Kaydanov, U. Laor, A. Gupta, T.R. Ohno, B. McCandless, "AC Characterization of Grain Boundary Electronic Properties in CdTe Thin Films", *NCPV Program Review Meeting 2000*, April 2000, Denver, CO, pp 259-260.

3. A.Gupta, S. Townsend, V. Kaydanov and T.R. Ohno, "Comparison of Degradation in Vapor Transport- and Electro-Deposited CdTe Solar Cells with ZnTe:Cu/Au and Cu/Au Back Contacts", Ibid, pp. 271-272

4*. T.R. Ohno, "Photovoltaic Research at the Colorado School of Mines", Physics Department Colloquium, University of Colorado-Colorado Springs, October 22, 1999.

5*. A.Gupta, S. Townsend, T. Ohno, V. Kaydanov, "Degradation of CdS/CdTe Solar Cells: Cu:ZnTe/Au vs. Cu/Au Back Contact, Electrodeposited CdTe vs. First Solar CdTe", *National CdTe R&D Team Meeting*, NREL, Golden, CO, January 27-28, 2000.

6*. T. Ohno, V. Kaydanov, R. Collins, A. Gupta, M. Herndon, U. Laor, "Grain Boundary Properties: Observations at the Colorado School of Mines", Ibid.

7*. V. Kaydanov, P. Meyers, "Some Possible Effects of Grain Boundaries on Thin Film Cell Performance", Ibid.

8*. D.L. Young, T.J. Coutts, V.I. Kaydanov, W.R. Mulligan, "Direct measurement of Density-of-States Effective Mass and Scattering Parameter in Transparent Conducting Oxides Using Second-Order Transport Phenomena", *The Amer. Vac. Soc. 46th Int. Symp.*, Seattle, WA, 2000

9*. D.L. Young, T. Coutts, X. Li, J. Keane, V.I. Kaydanov, A.S. Gilmore, "Density-of-States Effective Mass and Scattering Parameter Measurements on Transparent Conducting Oxides using Second-Order transport Phenomena", *Mater. Res. Soc. Meeting*, Spring 2000

REPORT DOCUMENTATION PAGE

Form Approved
OMB NO. 0704-0188

1. AGENCY USE ONLY (Leave blank)	2. REPORT DATE	3. REPORT TYPE AND DATES COVERED
	March 2001	Annual Technical Report, Phase II 16 May 1999 – 13 May 2000

4. TITLE AND SUBTITLE
Process Development and Basic Studies of Electrochemically Deposited CdTe-Based Solar Cells; Annual Technical Report, Phase II, 16 May 1999–13 May 2000

5. FUNDING NUMBERS
C: XAK-8-17619-28
TA: PVP15101

6. AUTHOR(S)
V.I. Kaydanov and T.R. Ohno

7. PERFORMING ORGANIZATION NAME(S) AND ADDRESS(ES)
Colorado School of Mines
Golden, Colorado 80401

8. PERFORMING ORGANIZATION REPORT NUMBER

9. SPONSORING/MONITORING AGENCY NAME(S) AND ADDRESS(ES)
National Renewable Energy Laboratory
1617 Cole Blvd.
Golden, CO 80401-3393

10. SPONSORING/MONITORING AGENCY REPORT NUMBER
NREL/SR-520-29956

11. SUPPLEMENTARY NOTES
NREL Technical Monitor: Bolko von Roedern

12a. DISTRIBUTION/AVAILABILITY STATEMENT
National Technical Information Service
U.S. Department of Commerce
5285 Port Royal Road
Springfield, VA 22161

12b. DISTRIBUTION CODE

13. ABSTRACT *(Maximum 200 words)* This project, carried out at the Colorado School of Mines, addresses long-term research and development issues related to polycrystalline thin-film solar cells. Our general research approach is based on combining activities aimed at improving cell performance and stability with activities aimed at increasing our fundamental understanding of the properties of materials making up the cells: CdTe, CdS, multilayer back-contact, and transparent conducting oxide (TCO) from contact. We emphasize the relation between structural and electronic materials properties and various processing procedures, as well as the microscopic mechanisms responsible for the cell performance and its degradation. Section 1 presents studies of degradation under stressing of the cells with differently processed CdTe and different back contents. Section 2 presents studies of deep traps in the electrodeposited (ED) CdTe cells performed in collaboration at NREL. Section 3 reports studies of the spectral dependencies of photocurrent, and their spatial distribution over the cross-section of the ED CdTe cells were performed using near-field scanning optical microscopy (NSOM). Section 4 discusses the impedance spectroscopy of CdTe and CdS thin films. Section 5 presents studies of band spectrum and electron scattering in transparent conducting oxides. Appendices present data on personnel involved in the studies, laboratory improvements, and publications.

14. SUBJECT TERMS
PV; polycrystalline thin-film solar cells; CdTe; CdS; multi-layer back contact; transparent conducting oxide (TCO); dopant compensation; degradation of cells; electromigration and transformation; deep traps; near field scanning optical microscopy; impedance spectroscopy; band spectrum; electron scattering

15. NUMBER OF PAGES

16. PRICE CODE

17. SECURITY CLASSIFICATION OF REPORT	18. SECURITY CLASSIFICATION OF THIS PAGE	19. SECURITY CLASSIFICATION OF ABSTRACT	20. LIMITATION OF ABSTRACT
Unclassified	Unclassified	Unclassified	UL